

1

Surface Energetic Principles for Moisture Storage in Porous Materials

1.1 Introduction

Most natural mineral materials, with the exception of crystals, have a pore system whose pores can range from very fine nanometer (nm)-sized pores to the millimeter (mm) range. A recognized **classification of pore sizes** has been made by International Union of Pure and Applied Chemistry (IUPAC). In the 2015 update of the 1985 report [1]. In this paper, the pores are classified into macropores, mesopores, and micropores.

Building materials such as natural stone, brick and especially concrete cover the full pore size range mentioned. Concrete materials usually contain a substantial concentration of particularly fine pores, which are classified in the group of nanopores.

These porous materials can therefore store liquids in the pore system, especially water, which can be carried in vapor form or in liquid form via surface forces.

The capillary absorbed liquid content is measured in $[\text{kg}/\text{m}^3]$ or in $[\text{m}^3/\text{m}^3]$, the velocity usually with good approximation as $W = ww \cdot \sqrt{t}$ in $[\text{kg}/\text{m}^2]$ with the material coefficient ww in $[\text{kg}/(\text{m}^2 \cdot \text{s}^{0.5})]$ when constant fluid supply is ensured.

To describe the storage of liquid from vapor uptake, the resulting water content is presented in the form of **sorption isotherms** as a function of the external relative humidity φ or after converting the relative humidity to the corresponding capillary pressure in the material.

In a number of (building) materials, such as brick products, a portion of the pores is so large that it is no longer filled by vapor adsorption, even at about 100% relative humidity. These pores can then only be filled capillary by external liquid-water supply. This water fraction is called the superhygroscopic range of total water uptake. In such cases, the total moisture storage is described by the so-called **moisture storage function**.

As indicated in the schematic moisture storage function in **Figure 1.1a**, many authors allow the hygroscopic range of the moisture storage function to extend only to about 98% relative humidity, when in fact it must be defined to about 100% RH. The reason for this is the difficulty of precisely setting the moisture and measuring it accurately in this 100%-near range. If the material also contains large pores that cannot be filled by capillary action – for example, air pores – the associated pore volume,

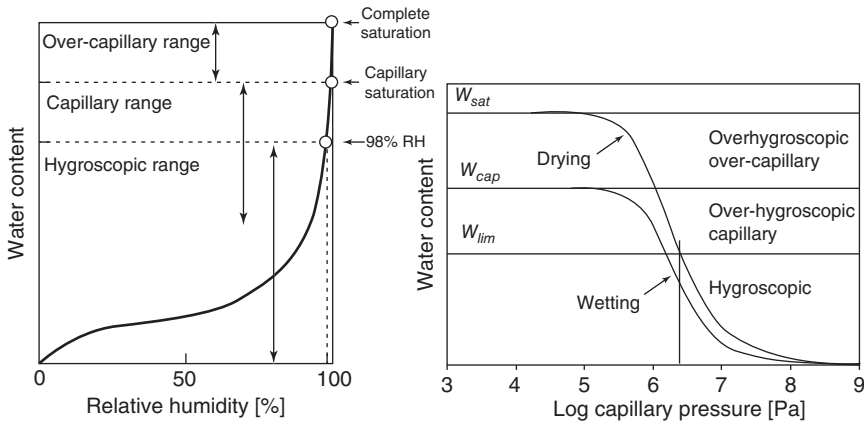


Figure 1.1 (a) Model of the water-storage function for cement-bound material. Source: Adapted from Fagerlund [2] and Eriksson et al. [3]. (b) Sample moisture adsorption and desorption storage functions for building materials as a function of capillary pressure p_c . Source: Carmeliet and Roels [4]/Sage Publications.

which can usually only be filled under pressure, is assigned to the **overhygroscopic range**.

The curve region above 98% RH can be determined using the pressure plate experiment [5, 6], and Espinosa–Franke [7] as a so-called suction stress curve depending on the applied capillary pressure. The mutual conversion of φ in p_k is done with Eq. (1.1). In this way, moisture-storage functions can also be represented completely as a function of p_k instead φ as, for example, by Carmeliet in **Figure 1.1b**. At 98% relative humidity, the associated capillary pressure is $p_k = 2.7 \cdot 10^6$ [Pa].

This means that in **Figure 1.1a,b** only the lower section of the curves (in the hygroscopic region) was determined by sorption measurements. The overhygroscopic ranges thus concern additional capillary water absorption as well as further water absorption under pressure also with (partial) filling of **the processing-related or artificially inserted air pores**.

Using the Eq. (1.39) explained in more detail in Section 1.3.2, the vapor pressure dependence of the adsorption and desorption curves can be converted to the corresponding dependence on the associated capillary pressure in [Pa] as follows:

$$p_k = R_D \cdot T \cdot \rho_W \cdot |\ln(\varphi)| \tag{1.1}$$

Sorption tests on building materials, in particular cement-bound materials, yield desorption curves that deviate significantly from the adsorption curves or moisture storage functions during water absorption. The reason for this behavior will be discussed in more detail in Section 4.6. Measurements by, for example, Feldman and Serada [8] or Ahlgren [9] have already made this clear in 1968 and 1972, see **Figure 1.2a,b**. The measurements also show that a transition between an absorption and desorption curve, or vice versa, occurs on a “short path,” **referred to as scanning loops or scanning isotherms**. The main focus of Chapters 2, 3,

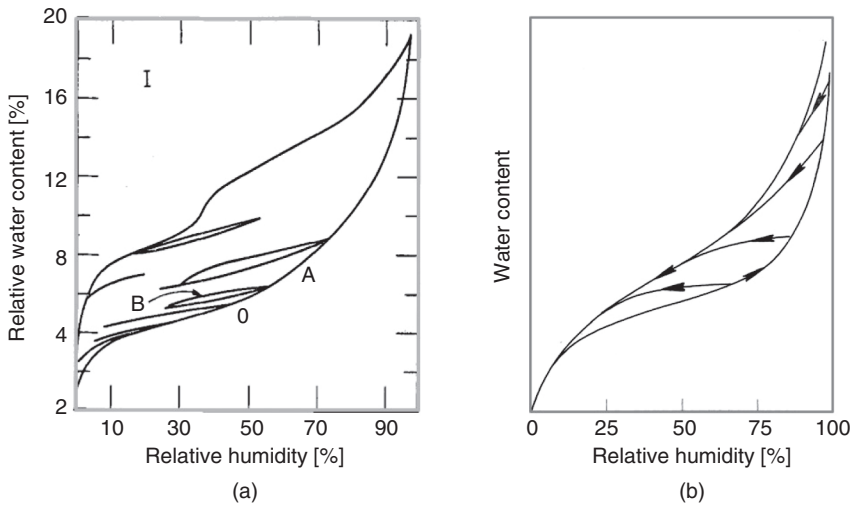


Figure 1.2 (a) Adsorption and desorption isotherms and scanning loops measured on HCP of Portland cement $WZ = 0.80$. Source: Feldman and Sereda [8]/Springer Nature. (b) Principle course of moisture storage functions including scanning isotherms of building materials. Source: Ahlgren [9]/Lund Institute of Technology/CC BY 4.0.

and 4 will be to show the effects of this behavior on the moisture transport and the moisture household of corresponding material bodies.

It will be shown that the individual moisture storage functions may have a fundamental importance for the moisture balance of porous materials and the modeling of moisture transport.

1.2 Surface Energy and Spreading of Liquids on Solid Surfaces

Since pore water within moist porous bodies is transported by capillary pressure (and vapor pressure) in the presence of sufficiently fine pores, and therefore capillary pressure is a crucial quantity with respect to moisture transport, the origin of capillary pressure within the pore system is first addressed. This first requires **explanations of the role of the surface energy** of the substances involved.

1.2.1 Explanations on Surface Energy and Surface Tension

The molecular arrangement on a water surface surrounded by air is shown schematically in **Figure 1.3**. In contrast to the interior of water, where the molecules are surrounded by similar molecules in all spatial directions and therefore force effects between the molecules cancel each other out in the summation, the surface lacks balancing molecular partners on the air side.

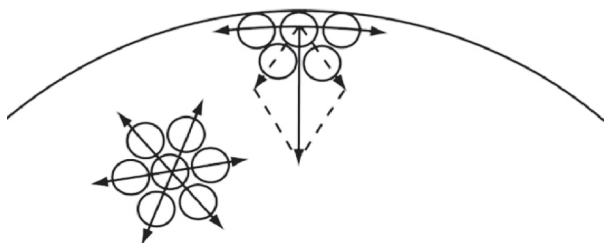


Figure 1.3 Orientation of water molecules and schematic representation of the attractive forces at the liquid surface, by D. Drummer, Erlangen-Nürnberg, Germany.

Therefore, a molecular arrangement is formed at the surface, which leads to inwardly directed cohesive forces (hydrogen bonds) and force effects in the surface plane.

To increase the liquid surface area, work must be done to overcome the cohesive forces of a considered amount of water while the volume remains unchanged. The work to be done per unit area to increase this surface area A is called the surface energy γ_{LV} [LV means liquid versus air], **here abbreviated as γ_L** , corresponding to Eq. (1.2) in differential formulation:

$$\gamma_L = \frac{dW_{surface(L)}}{dA} \quad \left[\frac{\text{Nm}}{\text{m}^2} = \frac{\text{N}}{\text{m}} \right] \quad (1.2)$$

$$F = 2 \cdot b \cdot \gamma_L \quad [\text{N}] \quad \Rightarrow \quad \gamma_L = \frac{F}{2 \cdot b} \quad \left[\frac{\text{N}}{\text{m}} \right] \quad (1.3)$$

Using Figure 1.4, it can be shown how surface energy can be determined by surface enlargement in a model experiment:

A water membrane (producibile by addition of surfactant) of dimension $b \cdot s$ is stretched by δs with force F . The surface (front and back) increases by $2 \cdot b \cdot \Delta s$.

The work done to increase the surface $\Delta W_{surface(L)}$ is given in **Figure 1.4** using Eq. (1.2).

The displacement work is $\delta s \cdot F$ (δs and F measured).

The formulations of the work $\Delta W_{surface(L)}$ and $\Delta W_{boundary}$ describe the same change in the sample and therefore must be equal in magnitude. Thus,

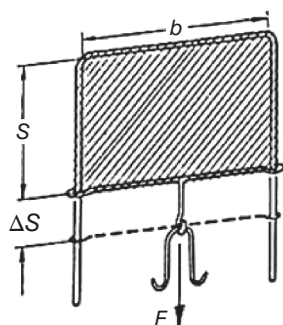


Figure 1.4 Testing Model : Measuring the surface energy and surface tension by the work of displacement Δs and the boundary force F on a (soap)-watermembrane.

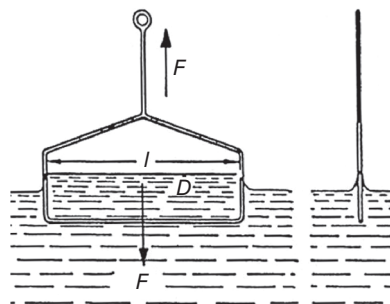
$$\Delta W_{surface(L)} = 2 \cdot (\Delta s \cdot b \cdot \gamma_L) \quad [\text{Nm}]$$

$$\Delta W_{boundary} = \Delta s \cdot F \quad [\text{m} \cdot \text{N}]$$

$$\Delta W_{surface(L)} = \Delta W_{boundary}$$

Figure 1.5 Measuring of the surface tension by

the bracket-method $\eta_L = \frac{F}{2 \cdot l} \left[\frac{\text{N}}{\text{m}} \right]$.



Eq. (1.3) yields the magnitude of the (specific) surface energy of the surfactant-added water. It can be seen that the special molecular orientation or the resulting surface cohesion in surface plane of the water membrane can introduce an edge force leading to an increase of the surface area, which is called the surface stress. From Eq. (1.3), it can be derived at the same time that the boundary force F related to the unit of the boundary length in [m] corresponds to the surface energy γ_L of the liquid.

The true value γ_L for non-surfactant water can be determined fairly accurately with the experiment shown in **Figure 1.5**, in which a wire stretched in a stirrup structure is lifted out of a water surface via a precision balance. The water surface around the wire is lifted until it breaks off when the maximum force F is reached. The surface energy of water is $0.07275 \text{ [Nm/m}^2 = \text{N/m]}$ at 20°C , correspondingly 72.75 [mN/m] .

The examples of surface stress measurements shown in **Figure 1.6** illustrate the shapes that water surfaces can attain largely due to surface stress alone. Instead of the bracket test, the Noüy method or the Wilhelmy method are predominantly used; compare **Figure 1.6** and Welcome to DataPhysics-Instruments [10].

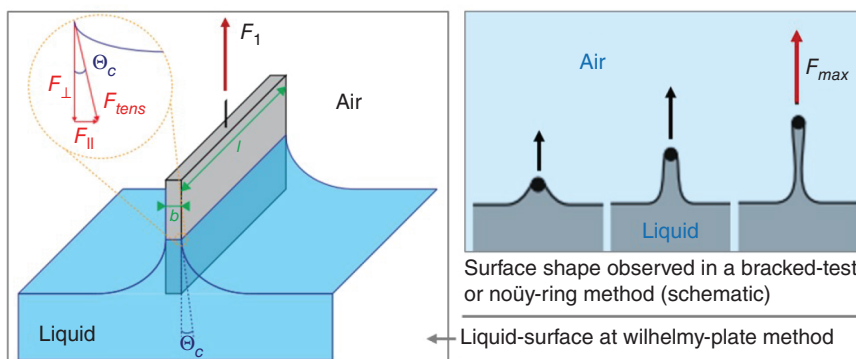


Figure 1.6 Measuring surface tension and corresponding liquid surface shapes by two different methods [10]. **Left:** Situation during a Wilhelmy-plate test. **Right:** Three states of the film surface during a bracket test (compare **Figure 1.5**) or with a ring-shaped wire during a Noüy test.

In the Nouÿ method, a ring-shaped wire is immersed and then drawn. A high-speed camera shows that in this process, the water surface takes on the shapes sketched on the right in **Figure 1.6** as the pulling force F increases. From the maximum tensile force F_{max} , the surface energy of the liquid is then calculated according to Eq. (1.3), corresponding to the Wilhelmy method.

1.2.2 Dependence of Surface Energy of Water on Temperature, on Relative Humidity of Air, and for Aqueous Salt Solutions

Results on the dependence of the surface energy of water on the relative humidity of the surrounding air were apparently first reliably determined in 2012 by Pérez-Díaz et al. [11], supplemented in 2017 by investigation results by Portuguez et al. [12]. Up to now, obviously, no corresponding results could be determined with capillary suction tests or on drops on flat material surfaces due to the mutual influence of liquid and solid or the resulting influences by simultaneous water evaporation.

As a new measuring method, Pérez-Díaz et al. and Portuguez et al. developed the **method of hanging drops** in climatic chambers combined with precise drop shape measurements via microscopy and image analysis.

The following **Figure 1.7a** shows the variation of the surface energy γ_L at 100% RH as a function of temperature in comparison to the already known behavior as a confirmation of the measurement methodology used. **Figure 1.7b** contains the results for different relative humidities at different temperatures. This shows, for example, that at 20 °C and 20% RH, the value of γ_L is about 5% larger than at 100% RH.

The dependence of surface energy on temperature at 100% RH can be calculated by the following Eq. (1.4). At 60 °C, $\gamma_w = 0.067$ [Nm/m²].

$$\gamma_w(\vartheta) = 0.07275 \cdot (1 - 0.002 \cdot (T_\vartheta - 293)) \quad (1.4)$$

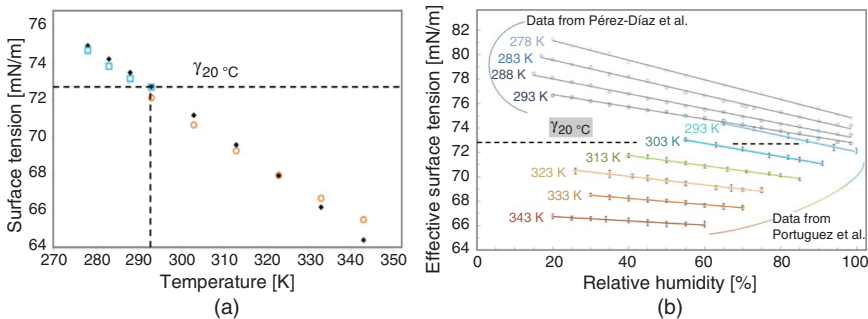


Figure 1.7 Measurement results for the surface energy of water as a function of ambient relative humidity and temperature, basic diagrams from Portuguez et al. [12] with data from Pérez-Díaz et al. [11] (a) Dependence of the surface energy at 100% RH as a function of temperature, comparison of the measured values of Portuguez (red circles) and of Pérez-Díaz (blue circles) with previous tabulated measured values (black signs). (b) Dependence of surface energy on relative humidity and temperature.

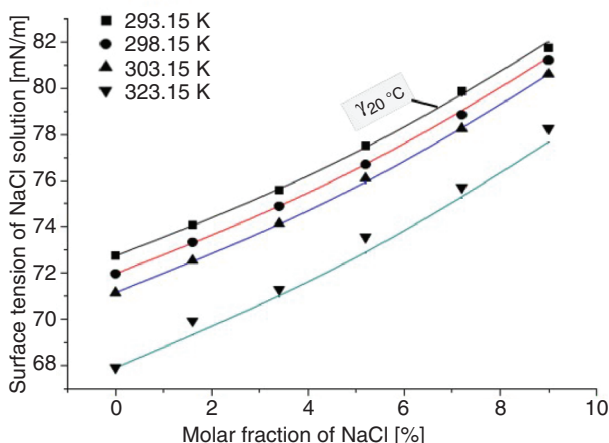


Figure 1.8 Surface tension of aqueous sodium chloride solution at 15–35 °C. Source: Chen et al. [13]/with permission of Elsevier.

According to American National Institute of Standards and Technology (NIST), γ_w at 100% RH and 100 °C: $\gamma_w \approx 0.059$ and at 200 °C: $\gamma_w \approx 0.037$ [Nm/m²]. The surface energy becomes zero at the critical point of water at 373 °C.

Furthermore, it is necessary to ask to what extent the surface energies change for aqueous salt solutions or electrolytes. For limited-concentration solutions, H. Chen et al. [13] presents a “Gibbs phenomenological surface-phase” method for numerous salts. **Figure 1.8** shows results from this publication for sodium chloride and sodium sulfate solutions. The relatively limited influence up to salt contents of 1 [mol/kg] can be seen.

1.2.3 Spreading of Liquids on a Solid Surface

The ability of a liquid to wet a solid depends largely on the surface energies of the substances involved. Therefore, **the surface energies of solids** are also important.

These surface energies can only be measured indirectly at room temperature using drops of test liquids whose surface energies are known. Contact angle measurement is usually used, in which the angle of inclination or the edge angle to the solid surface is determined and the surface energy is derived from this, compare for example Kinloch [14]. Also, so-called test inks allow an approximate determination of the energetic surface states.

For the evaluation of the results, the following considerations are important:

Is defined first

γ_L = **specific surface energy of the liquid** in the environment air plus vapor.

γ_{SV} = **specific surface energy of the solid** in the environment air plus vapor, as well as

γ_{SL} = **specific interfacial energy**, which can exert a separating effect in the interface between the liquid in contact and the solid due to the different molecular nature.

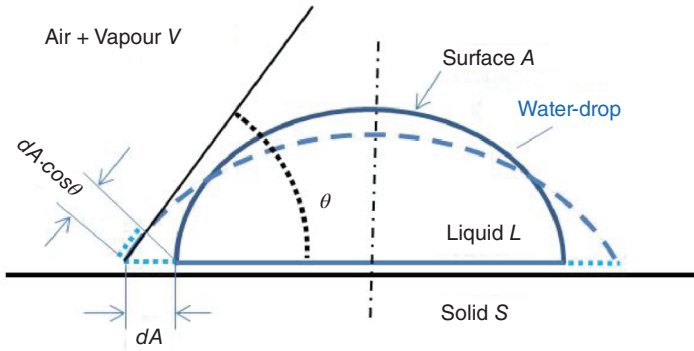


Figure 1.9 Incremental progress dA of a water droplet (L) on a solid surface (S) shortly before reaching the energetic balance of the surface energies involved.

For an understanding of the following relationships, we refer to **Figure 1.9** of a partially contacting droplet with total surface area of A and a given volume.

The spreading of the droplet (L) on the solid surface (S) occurs, if the preconditions are met, due to the effect of attractive forces between the liquid and the solid, which are able to overcome the surface tension of the liquid when the contact area is increased.

The spreading comes to a stop when a minimum of the total energy of the ongoing process is reached. **Figure 1.9** represents the situation just before this standstill:

The already existing contact area between (L) and (S) still increases by the fraction dA . On the air side of the contacting droplet, the surface area is thus approximately increased by the value $dA \cdot \cos\theta$. In total, the droplet surface area thus increases by $dA + dA \cdot \cos\theta$. For this, the following work must be done on the drop side:

$$dW_{\text{surface}}(L) = \gamma_L \cdot (dA + dA \cdot \cos(\theta)) \quad (1.5)$$

At the same time, adhesion energy is released in the area of contact area increasing dA :

$$dW_{\text{Adh}}(SL) = -dA \cdot (\gamma_L + \gamma_{SV} - \gamma_{SL}) \quad (1.6)$$

Here γ_{SL} expresses that there is not a full saturation of the surface energy in contact but is reduced by the fraction $\gamma_{SL} \cdot dA$. At equilibrium:

$$dW_{\text{surface}}(L) + dW_{\text{Adh}}(SL) = 0 \quad (1.7)$$

It follows

$$(1 + \cos(\theta)) \cdot \gamma_L + \gamma_{SL} - \gamma_L - \gamma_{SV} = 0 \quad (1.8)$$

and for the boundary angle θ the well-known Young equation follows after the transformation:

$$\cos(\theta) = \frac{\gamma_{SV} - \gamma_{SL}}{\gamma_L} \quad (1.9)$$

At $\cos\theta = 1$ or $\theta = 0$ complete wetting or dissolution of the drop takes place.

The surface energies present now allow **statements about the dispersion behavior of different liquids on different surfaces**. This also determines whether a liquid can penetrate a pore system. The measurement of the contact angle in the drop test provides at least approximate information on this. If the contact angle is about 90° , $\gamma_{SL} \approx 0$. This results in a “neutral” behavior of the given liquid on the given solid surface. No capillary water absorption takes place in this case. In order that capillary takes place, the angle θ must be appreciably less than 90° .

According to the following equation by van Honschoten et al. [15], spreading occurs for a solid–liquid combination when the value S is positive:

$$S = U_{dry}^{substrate} - U_{wet}^{substrate} = \gamma_{SV} - (\gamma_{SL} + \gamma_{LV}) \quad (1.10)$$

1.2.4 Determining the Surface Energies of Solid Surfaces

For mineral materials used in construction, the contact angle is usually less than 90° , unless the surface has been modified, for example, by a hydrophobizing measure. Kaolin has a surface energy of about 500–600 [mN/m]; HPC concretes with aggregate from granodiorite and from granite with a compressive strength of about 130 [MPa] have, according to Barnat-Hunek $\gamma_S = 1000$ to 1800 [mN/m] [16] and a contact angle of about 10° to 30° when wetted with water at 22°C , resulting in capillary water absorption into a pore system.

Calcium carbonate has a surface energy of only $\gamma_S = 75$ –80 [mN/m], so that largely standing water droplets can be expected on such surfaces.

Plastics, paints, and waxes have a γ_S of 25–40 [mN/m], so that no spreading of water can take place on these surfaces, which is very well seen, for example, on waxed car bodies. Teflon exhibits a γ_S of about 20 [mN/m].

In contrast, ethanol or isopropanol, for example, with surface energies of 22 or 23 [mN/m] on mineral surfaces always show a contact angle close to 0° , i.e. complete spreading and a strong readiness for capillary penetration into capillary pores.

Metal alloys also usually have very high surface energy, γ_{SV} -values of metals can be taken from Kumikov and Khokonov [17]. Nevertheless, with respect to adhesion, adequate surface pretreatment is especially important for metals.

If, in the case of “unknown” solid surfaces, their surface energy γ_S is needed, however, it cannot be determined only by determining a boundary angle with a known liquid. A more accurate determination of the surface energy can be made by at least two edge angle measurements with two different test liquids with different, known **polar interaction fractions** γ_L^p (for example, from hydrogen bonding) and **dispersive fractions** γ_L^d (from van der Waals forces).

The surface energy γ_{SV} of the solid as well as the interfacial energy γ_{SL} can then be determined from the results of the boundary angle measurements according to the accepted OWRK method of Owens, Wendt, Rabel, and Kaelble, compare Yuan and Lee [18], Lauth and Kowalczyk [19], and Barnat-Smarzewski and Smarzewski [16].

In Literature [20], measurement and calculation results from two institutes are reported by Cwikel et al., in which the performance of five different computational

models for determining the surface energy of solids is investigated. For this purpose, the contact angles of selected test liquids on 42 different solid surfaces are measured and compared with the predictions of the computational models.

1.3 Basic Equations for Liquid Absorption in Material Pores

1.3.1 Liquid Absorption in Pores by Effect of Surface Energies

Liquid is also drawn into the inner surface of material pores by the effect of surface tension. The finer the pores, the greater the depth of penetration or rise relative to gravity. In such pores, the liquid is transported as in a tube. This is traditionally shown by the liquid rise height in a cylindrical capillary pore.

1.3.1.1 Derivation of the Capillary Rise via the Adhesion Works and the Potential Energy in Capillaries

The adhesion works in a standing cylindrical capillary are for the rise height h :

$$W_{surface}(h) = +2 \cdot \pi \cdot r_{pore} \cdot \gamma_L \cdot h + W_{surface}(0) \quad (1.11)$$

$$W_{Adh}(h) = -(\gamma_L + \gamma_{SV} - \gamma_{SL}) \cdot 2\pi \cdot r_{pore} \cdot h - W_{Adh}(0) \quad (1.12)$$

The potential energy to be overcome is:

$$E_{pot}(h) = +r_{pore}^2 \cdot \pi \cdot \rho_L \cdot g \cdot \frac{h^2}{2} + E_{pot}(0) \quad (1.13)$$

At equilibrium is

$$\frac{dW_{surface}(h)}{dh} + \frac{W_{Adh}(h)}{dh} + \frac{E_{pot}(h)}{dh} = 0 \quad (1.14)$$

From this follows, shortened by $2 \cdot \pi \cdot r_{pore}$:

$$-(\gamma_{SV} - \gamma_{SL}) + r_{pore} \cdot \rho_L \cdot g \cdot \frac{h}{2} = 0 \quad (1.15)$$

Using Eq. (1.9), this gives the relationship for the achievable height due to adhesion work in a cylindrical capillary:

$$h_{max} = \frac{2 \cdot \cos(\theta) \cdot \gamma_L}{r_{pore} \cdot g \cdot \rho_L} \quad (1.16)$$

If instead slit pores with a constant spacing of the pore surfaces of $d = 2 \cdot r_{pore}$ are present, the result for the rise height is

$$h_{Slit,max} = \frac{2 \cdot \cos(\theta) \cdot \gamma_L}{d \cdot g \cdot \rho_L} \quad (1.17)$$

If $d = 2 \cdot r_{pore}$ gives $h_{slot} = 1/2 \cdot h_{cap}$. At this point, we refer the reader to Section 1.3.1.3, where a more general derivation of the fluid uptake in pores due to adhesion work is described.

1.3.1.2 Capillary Pressure in Cylindrical Pores and in Slit Pores

The transport in capillary pores or slit pores caused by the surface energy creates a tensile stress below the menisci in the pores, which is called capillary pressure. As a result of the previous explanations, the resulting capillary pressure can be simply represented according to **Figure 1.10**. The water column of the pores resp. pore filling is further pulled by the effect of the surface energies resp. the corresponding surface tension at the wall of the pores. In dependence of the existing edge angle θ from Eq. (1.9), the force component f_{cap} in [N/m] is now generated there in the pore direction.

$$f_{cap} = \gamma_L \cdot \cos(\theta) \tag{1.18}$$

For a cylindrical capillary pore with a given perimeter, the resulting total force follows to

$$F_{cap} = f_{cap} \cdot 2\pi \cdot r_{pore} \tag{1.19}$$

The resulting capillary pressure p_{cap} cannot be exceeded by the surface energy alone because of the limitation of the surface tension to γ_L . The capillary pressure is then (when the surrounding air pressure is not taken into account)

$$p_{cap}(r) = \frac{F_{cap}}{\pi \cdot r_{pore}^2} = \frac{2 \cdot \gamma_L \cdot \cos(\theta)}{r_{pore}} \text{ [Pa]} \tag{1.20}$$

In the presence of slit pores with d = surface distance of the pore walls, the following results instead

$$p_{cap}(d) = \frac{2 \cdot \gamma_L \cdot \cos(\theta)}{d} \text{ [Pa]} \tag{1.21}$$

When $d = 2 \cdot r_{pore}$, $p_{cap}(d)$ is only half as large as for a cylinder pore, according to Eq. (1.20).

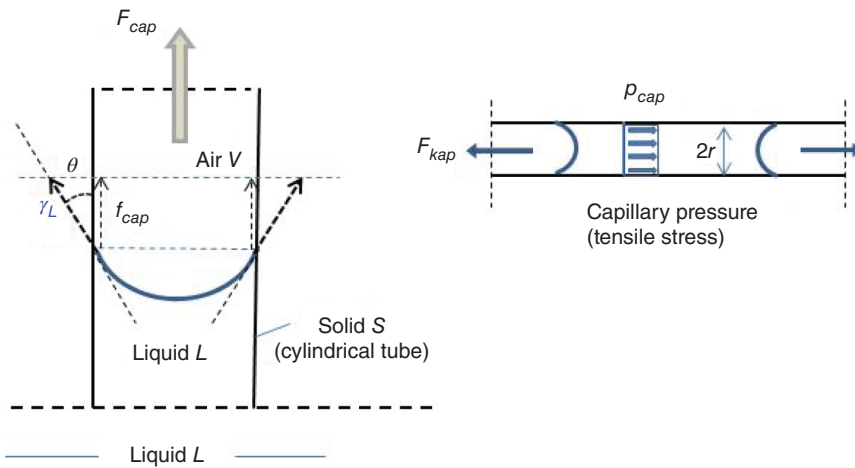


Figure 1.10 Formation and definition of capillary pressure in a cylindrical pore during water absorption.

The influence of changing temperatures and possible salinity on γ_L has been given previously.

1.3.1.3 Capillary Pressure as a Cause of Fluid Transport and Rise Height in a Capillary Pore

From Extrand and Moon [21], using simple water absorption experiments on glass capillaries, it is shown that the derivation of the rise height in capillary pores in terms of surface work and potential energy presented in Section 1.3.1.1 leads to an unjustified formal restriction on the applicability of the Eq. (1.16).

According to this equation, varying ratios of surface energies along the capillary pore and a varying pore cross section, for example, a larger pore radius in the lower part of the capillary, should also lead to the same riser height (1.16). Extrand and Moon [21] concludes that the capillary pressure at the head of the water column in the capillary is responsible for the increase, independent of the other parameters. In fact, this can be shown and somewhat specified in the following way:

Instead of (1.11) and (1.12), let be written only the local increase of the surface energy fractions or work fractions of the liquid surface $\Delta W_{surface}$ and the solid surface ΔW_{Adh} in the region of the pore radius r_{pore}

$$\Delta W_{surface} = +2 \cdot \pi \cdot r_{pore} \cdot \gamma_L \cdot \Delta h \quad (1.22)$$

$$\Delta W_{Adh} = -(\gamma_L + \gamma_{SV} - \gamma_{SL}) \cdot 2 \cdot \pi \cdot r_{pore} \cdot \Delta h \quad (1.23)$$

The resulting energy sum does the work of raising the corresponding liquid level. The corresponding mechanical work portion force \cdot displacement results at the considered radius from the product of the pore cross-sectional area and the hydraulic stress acting in the cross-section times the displacement Δh . For example, the surface of the advancing fluid has the shape of a meniscus. The associated mechanical work is then, with the hydraulic (tensile) stress p_{cap}

$$\Delta W_{meniscus} = r_{pore}^2 \cdot \pi \cdot p_{cap} \cdot \Delta h \quad (1.24)$$

At equilibrium is

$$\Delta W_{surface} + \Delta W_{Adh} + \Delta W_{meniscus} = 0 \quad (1.25)$$

From this follows, shortened by δh and $2 \cdot \pi \cdot r_{pore}$, with $\gamma_{SV} - \gamma_{SL} = \cos(\theta) \cdot \gamma_L$ the relation

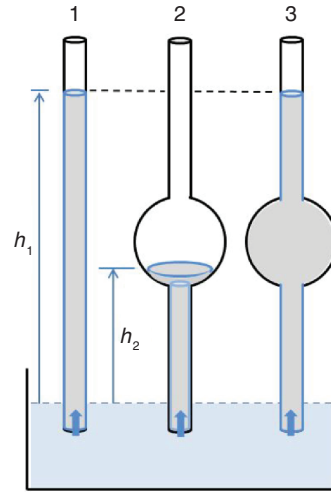
$$p_{cap} = \frac{2 \cdot \gamma_L \cdot \cos(\theta)}{r_{pore}} \quad [\text{Pa}] \quad (1.26)$$

With the suction stress p_{cap} , the fluid bulk density ρ_L , and the acceleration due to gravity g , the hydraulic potential or the fluid pressure head is given by

$$h = \frac{p_{cap}}{\rho_L \cdot g} \quad (1.27)$$

Figure 1.11 shall schematically illustrate the relationship between the effect of capillary pressure and gravity in different capillaries. h_1 is the rise height in capillary 1 with the associated capillary pore radius r_1 according to Eq. (1.16) resp. (1.27).

Figure 1.11 Possible equilibrium suction heights for three model capillaries with identical inner radius in the upper region.



If the capillary has a radius extension, for example, in the form of a spherical pore, the liquid uptake stops when entering the spherical pore according to the associated radius extension, resp. the lower capillary pressure (capillary 2 in 1.11). If, on the other hand, the sphere pore is filled with water by some action in the sense of a continuous pressure connection to the surface, the rise height reaches the suction height h_1 for a capillary radius $r_3 = r_1$.

It is to be noted that only the adhesion work in the area of the front meniscus and the capillary pressure there (as suction force) lead to the progress of the water column.

If **capillary condensation** takes place at the front of the capillary pore due to the boundary conditions (pore radius and vapor pressure, compare Sections 1.3.2 and 1.4.5), liquid is added there accordingly, but the capillary head h_1 is not increased.

When the capillaries are horizontal or there is no gravity (but water contact at the base), the capillary is completely filled by the adhesion work up to the head, regardless of its length.

1.3.2 Pore Filling by Capillary Condensation

In an empty pore system of a dried material, if the external vapor pressure is increased from very small pressures to saturation pressure p_{sat} , the vapor diffusing into the pores leads to sorption layer thicknesses at the pore walls corresponding to the associated “base isotherm.” For water vapor, this is the Eq. (1.50) resp. **Figure 1.15a**. These sorption liquid layers are also called liquid films.

Practical experience confirms that fine-porous materials have moisture contents that correlate with the moisture content of the surrounding air. In the following, it will be shown again why this must be so.

As a reminder, the general gas equation for ideal gases is written first.

$$p = \frac{n}{V_{ges}} \cdot R \cdot T \quad (1.28)$$

There is p = Gas pressure in [Pa], $R = 8.31$ [Nm/(K·mol)] = General gas constant, and n = Number of moles of gas in V_{ges} .

If $n = 1$ follows $V_{ges} = \bar{V}$ = Molar volume = 24.46 [l/mol] under thermodynamic standard conditions 25 °C and 101.3 [kPa] and 22.414 [l/mol] under standard conditions 0 °C and 101.3 [kPa].

Equation (1.28) is also valid for the partial pressures of individual gas components in gas mixtures, for example also for the water vapor fraction in air.

Let the saturation concentration for water vapor in air be c_S . At 20 °C, $c_S = 17.3$ [g/m³]. In contrast, air weighs about 1170 [g/m³] under standard conditions. The partial pressure for water vapor in air is also:

$$p_S = c_S \cdot 0.462 \cdot T \quad [\text{Pa}] \quad (1.29)$$

Herein, 0.462 is the specific gas constant (independent of boundary conditions) for water vapor in [Pa·m³/(g·K)] and c_S in [g/m³]. Let p_S be the saturation partial pressure of water vapor in air. The temperature dependence is $\delta \geq 0$ °C.

$$p_{S(\delta)} = 288.58 \cdot \left(1.098 + \frac{\delta}{100}\right)^{8.02} \quad (1.30)$$

The vapor concentration is c_S in equilibrium with a (flat) water surface A_0 at a given temperature T_0 .

If the water surface is curved concavely, this leads to a higher relative concentration c_S with respect to the curved water surface A_1 . Expressed as relative concentration c_S/A is now $c_S/A_1 > c_S/A_0$, which is especially clear when imaging the inner surface of a sphere.

To maintain thermodynamic equilibrium, the liquid surface must absorb vapor molecules from the air in an effort c_S to reduce. In the initial plane state, the equilibrium between the phases of water and vapor in contact in confined space is as follows:

$$d\bar{G} = \mu_L \cdot dn_L + \mu_D \cdot dn_D = 0.$$

Since $dn_L = dn_D$ must be, it follows (at unchanged temperature and pressure) $\mu_L = \mu_D$.

When there is a curvature of the fluid surface, there is (due to the relationship between surface curvature and pressure) a change in pressure in the system. Here, first of all, the fluid pressure is meant.

$$d\mu = -S \cdot dT + V \cdot dp = V \cdot dp \quad \text{at } T = \text{const.}$$

On the part of the liquid, the change in chemical potential (or free enthalpy) to be compensated is compared to the initial state at a flat surface and at unchanged temperature, **with \bar{V} = molar volume of the liquid or water** and p_S the corresponding saturation pressure is

$$d\bar{G}_L = \bar{V} \cdot dp, \text{ respectively :} \quad (1.31)$$

$$\Delta \bar{G}_L = \int_{p_1}^{p_s} \bar{V}_L \cdot dp = -\bar{V}_L \cdot (p - p_s) \quad (1.32)$$

The **fluid pressure** can be $p \leq p_s$ or $p > p_s$. This depends on whether the pressure generated in the fluid is negative or positive. In the case of a cylindrical pore with a progressing meniscus of fluid filling in **Figure 1.10**, the fluid pressure should be assumed to be negative as a tensile stress.

In Eq. (1.20), r_{pore} is the radius of the cylindrical pore. In a circular–capillary, the pressure-transmitting meniscus has two main radii of curvature

$$r_{meniscus} = \frac{r_{pore}}{\cos(\theta)} \quad (1.33)$$

Inserted into Eq. (1.20), the Young–Laplace relation for a circular–cylindrical pore follows.

$$p_{cap(meniscus)} = \frac{2 \cdot \gamma_L}{r_{meniscus}} \quad [\text{Pa}] \quad (1.34)$$

In the plane initial state, $r_{meniscus} = \infty$ and thus $p_s = 0$ in Eq. (1.32). In the present case, p and hence δp is negative. From this follows for the fluid in the region of the meniscus

$$\Delta \bar{G}_L = \bar{V}_L \cdot \Delta p = -\bar{V}_L \cdot \frac{2 \cdot \gamma_L}{r_{meniscus}} = -\bar{V}_L \cdot \frac{2 \cdot \gamma_L \cdot \cos(\theta)}{r_{pore}} \quad [\text{J/mol}] \quad (1.35)$$

The enthalpy change of the liquid is followed by the corresponding **reaction of the vapor phase V**: From the saturation initial state c_s or p_s as the saturation pressure of the plane surface.

$$\Delta \bar{G}_V = \int_{p_1}^{p_s} \frac{R \cdot T}{p} dp = -R \cdot T \cdot \ln \left(\frac{p_1}{p_s} \right) \quad [\text{J/mol}] \quad (1.36)$$

where p_1 is the equilibrium saturation vapor pressure in the concave surface region.

From the requirement $\Delta \bar{G}_V = \Delta \bar{G}_L$ follows with Eq. (1.35) and $\bar{V}_L =$ mole volume of condensed liquid (18 [cm³] or 18/10⁶ [m³/mol] for water), the **Kelvin equation** given by $p_1 \leq p_s$ in the following formulation for concave surfaces:

$$r_{pore} = \frac{-\bar{V}_L \cdot 2\gamma_L \cdot \cos(\theta)}{R \cdot T \cdot \ln \left(\frac{p_1}{p_s} \right)} = \frac{M_\gamma}{\ln(\varphi)} \quad [\text{m}] \quad (1.37)$$

Therein, $p_1/p_s = \varphi_{ext}$ is the **external relative humidity** φ . The summary term M_γ (constant for given T) corresponds to Eq. (1.68).

Equation (1.37) indicates up to which pore radius, at a given vapor partial pressure p_1 a cylindrical pore is completely filled by condensation from the vapor entering the pore, denoted **capillary condensation**. Here, **for cylindrical pores with constant cross-section**, it is assumed that a meniscus supposed to be stationary is already present due to an interrupted water supply at the base of the capillaries, or in the case of an equilibrium situation as indicated in **Figure 1.10**. When exposed to an external relative vapor pressure of at least p_1 , in the curvature region of this

meniscus, the external vapor pressure becomes the saturation vapor pressure, with the consequence of condensation of the vapor present and pore filling.

If, for a given radius r_{pore} , the critical relative vapor pressure p_1 or the external relative humidity above which capillary condensation takes place is sought, the result is (Eq. (1.37) transformed):

$$\varphi_{ext} = e^{-\frac{\bar{V}_L \cdot 2\gamma_L \cdot \cos(\theta)}{R \cdot T \cdot r_{pore}}} \quad (1.38)$$

For materials with pore size distributions “small to large,” the entire material is filled only up to the pore size $r_1 = r_{pore}$ according to Eq. (1.37) by the vapor diffusing in from the outside.

The Kelvin Eq. (1.37) or the resulting Eq. (1.38) are generally valid also for curved concave liquid surfaces characterized by different principal radii of curvature, as well as **for pores with noncircular cross section.**

Combining the relations (1.37) and (1.20), we immediately obtain the relation between p_{cap} and $\varphi = p_1/p_S$

$$p_{cap} = -\frac{R \cdot T}{\bar{V}_L} \cdot \ln(\varphi) = R_D \cdot T \cdot \rho_W \cdot |\ln(\varphi)| \quad [\text{Pa}] \quad (1.39)$$

1.3.2.1 Extent of Validity of the Kelvin Equation

An important question is up to which lower pore radius the Kelvin equation is valid. The applicability is considerably limited by the charge distribution and the relation of the pore radius to the molecule size of the fluid under consideration. Numerous authors have commented on this issue in the past. **Matsuoka et al. [22]** perform atomic force microscopy (AFM) studies on liquid films between curved muscovite-mica surfaces at different relative humidities. They give a lower pore radius of $r = 1.5$ [nm] for (the polar) water, e.g. $r = 0.5$ [nm] for cyclopentanes.

Fifteen years later, **Kim et al. [23]** remark, based on measurements with more advanced atomic force microscope (AFM) technology, that a much lower boundary pore radius $r = 0.5$ [nm] for water can be assumed. They measure in the AFM apparatus at the curved contact surface of the samples capillary condensation down to the mentioned radius and evaluate the results based on the accepted Kelvin–Tolman theory, which gives a correction to Laplace’s equation for very small pore radii, compare also [24].

They emphasize explicitly that this result (also based on AFM studies) refers to the classical Kelvin equation according to Eq. (1.37).

If one includes the relation of Eq. (1.79) according to the representation in **Figure 1.22** or Section 1.4.5 and **Figure 1.15a**, then yields the corresponding real radius $r_R = 0.7$ [nm], which could then be called as the lower physically detectable pore radius for the applicability of the Kelvin relation.

1.3.3 Saturation Vapor Pressure at the Surface of Convex Shapes

In contrast to concave liquid surfaces, for example, at a meniscus in cylindrical pores, the saturation vapor pressure at convex external surfaces is increased by $p > p_S$, so that condensation of vapor occurs only at relative humidities $\varphi_1 > \varphi_S$.

It is then valid as liquefaction vapor pressure over an external surface (with the main curvature radii r). Instead of Eq. (1.38), the corresponding equation with reversed sign is then valid.

Since the relative vapor pressure is lower on such surfaces, faster evaporation or drying also takes place there.

In Section 1.4.6.2, the layer thicknesses of water molecules that can form by adsorption on concave or convex surfaces as a function of relative humidity are investigated.

1.3.4 Explanations of the Young–Laplace Equation for Stress on Curved Fluid Surfaces

The relation presented at the same time by Young and Laplace is as follows:

$$\Delta p = \gamma_L \cdot \left(\frac{1}{r_1} + \frac{1}{r_2} \right) \quad (1.40)$$

Equation (1.40) gives the mechanical relationship between the curvature of a nonplanar membrane-like surface, given by the two principal radii of curvature r_1 and r_2 , and the stress acting in the membrane plane γ_L in [N/m] and the pressure Δp in [N/m²] acting on the membrane surface (orthogonal).

This pressure can act from a liquid or a gas. Since a “water-membrane” is formed at the water surface, the surface can be treated with the Young Laplace relation (1.40). Since the membrane stress γ_L acts largely as a constant for water surfaces, Eq. (1.40) provides the relationship between the sum Δp of inside and possibly outside orthogonal pressure components on the surface and the curvature of the surface.

In the area of the concave meniscus in a cylindrical capillary pore the water pressure acts on the water side as a two-dimensional tensile stress, on the air side the air pressure (including vapor partial pressure). However, since the air pressure acts on the entire system, it is also present as a component on the “water side” of the meniscus and can therefore be disregarded (except in special cases).

This also indicates that for cylindrical capillaries with a constant cross-section, the vapor partial pressure does not play a role in meniscus formation, unless the sorption properties of the inner capillary-pore surface are affected by varying vapor pressure, which would manifest itself, for example in a change in the contact angle. There is no evidence for this in glass capillaries, for example. **In contrast, for capillaries with increasing pore radius** or pore systems with medium pore sizes increasing from “small to large” there is a clear relationship between the vapor partial pressure p_1 and the pore size or meniscus shape and thus the capillary pressure according to the Eqs. (1.37) and (1.34).

With reference to the Eqs. (1.33) and (1.34), results analogously to Eq. (1.40)

$$p_{cap(meniscus)} = \gamma_L \cdot \left(\frac{1}{r_{meniscus}} + \frac{1}{r_{meniscus}} \right) = \frac{2 \cdot \gamma_L}{r_{meniscus}} \quad (1.41)$$

Due to the limitation of the possible tensile stress in the “meniscus membrane” to γ_L , the possible capillary pressure (tension) is limited accordingly. The principal radii of

curvature $r_1 = r_2 = r_{meniscus}$ to be used for a circular–cylindrical capillary pore differ from the pore radius r_{pore} for a noncircular cross section according to Eq. (1.33).

Eslami and Elliott [25] have investigated **the exact shape of menisci under gravity and vapor pressure** in cylindrical capillaries mathematically in more detail by integrating Laplace’s equation and taking thermodynamic considerations into account.

Figure 1.12 shows from this work the results on the meniscus shape for the edge angle $\theta = 0$ and for varying edge angles. It can be seen that even the largest capillary pores in cement-bonded materials assumed to have circular cross-sections with radii on the order of 300 [nm] still exhibit pronounced curvature radii of nearly hemispherical shape in the presence of a edge angle of $\theta \approx 0$.

The edge angles on concrete surfaces were measured to be $10^\circ\text{--}15^\circ$. Even for such edge angles, the deviations from the hemisphere shape are small.

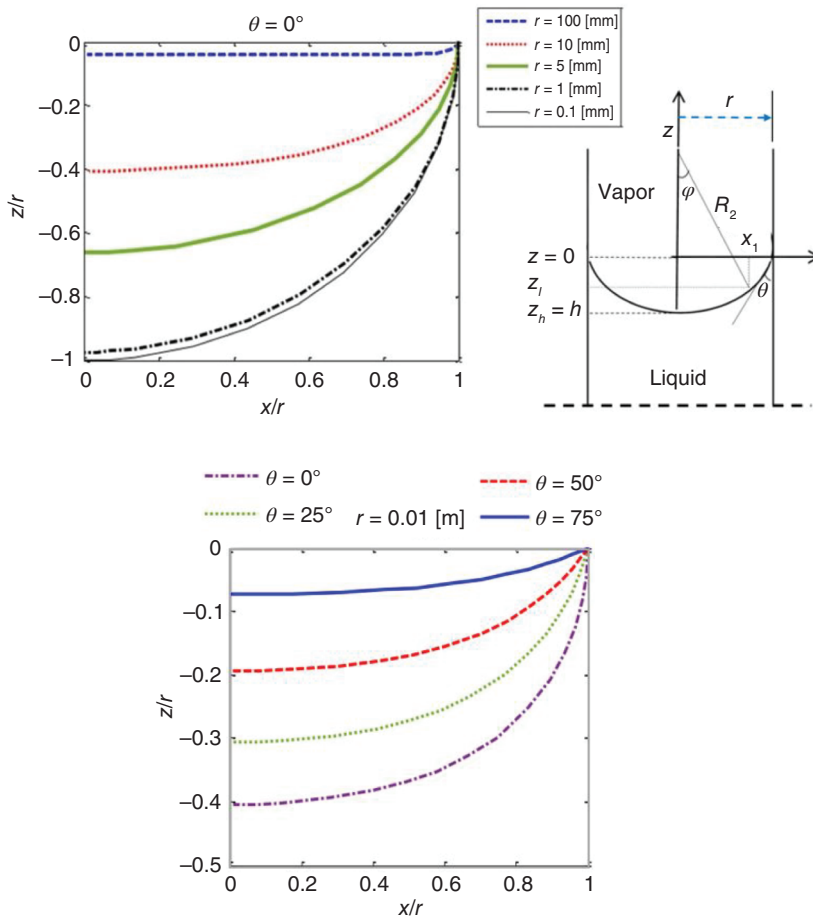


Figure 1.12 Meniscus shape in cylindrical pores as a function of pore radius at constant contact angle of 0° and influence of the contact angle at constant radius 10 [mm] (lower figure). Source: Eslami and Elliott [25]/Springer Nature/CC BY 4.0.

1.3.5 Application of Kelvin Equation to Floating Droplets

Spherically assumed **individual droplets in a vapor-supersaturated air** form different droplet sizes depending on the surrounding relative humidity φ_{ext} resp. degree of supersaturation, which can be determined by means of a fitted Kelvin equation.

In the droplet the internal pressure is positive in contrast to the liquid at a concave meniscus, furthermore at the “surface-membrane” of the droplets there is no more contact to a solid surface, so that the contact angle $\theta = 0$ and $\cos(\theta) = 1$ is.

The consequence is that in Eq. (1.32) p becomes $>p_0$ and from this follows instead of Eq. (1.34) for the fluid pressure

$$p_{drop} = \frac{2 \cdot \gamma_L}{r_{drop}} \quad (1.42)$$

and instead of Eq. (1.35) for the change of the chemical potential of the liquid

$$\Delta \bar{G}_L = +\bar{V}_L \cdot \frac{2 \cdot \gamma_L}{r_{drop}} \quad [\text{J/mol}] \quad (1.43)$$

Due to the increase of $\Delta \bar{G}_L$, a positive change of the chemical potential of the gas phase vapor must also result. However, in the Eq. (1.36), which also applies here, $p_1/p_S \geq 1.0$ must be used. From this follows the Kelvin equation adapted for free drops:

$$r_{drop} = \frac{+\bar{V}_L \cdot 2 \cdot \gamma_L}{R \cdot T \cdot \ln\left(\frac{p_1}{p_S}\right)} \quad [\text{m}] \quad (1.44)$$

In the absence of condensation nuclei or condensation-enabling surfaces in the vapor-containing air in question, supersaturation $\varphi > 1.0$ can be produced by supplying additional vapor or by cooling the air. Artificially, obviously, several times the saturation vapor pressure can be produced; in nature, normally only a few percent supersaturation is produced in the atmosphere. If the vapor meets condensation nuclei, a spontaneous condensation takes place, which immediately changes into an evaporation of the droplets if the pressure falls below $\varphi = 1.0$. The respective droplet sizes can be derived according to Kelvin from the respective local vapor concentration. **Overall, this is an unstable dynamical process that depends, among other things, on the transport velocity of the vapor molecules in the air.** Extensive research is still ongoing on this topic [see for example B. Waigand, University of Stuttgart, Germany].

1.3.6 Solubility of Gases in Water

The issue of solubility of gases, especially air in water, plays a role, for example, in the context of the behavior and influence of air of the filling of original air pores in the material by water. It is addressed in more detail in Section 4.5.5. Gases dissolve in water, for example, from the water surface under their present partial pressure. The relationship is described by Henry’s law. It indicates which dissolved gas concentration c_{w_i} of gas i results in water as a function of water temperature and partial

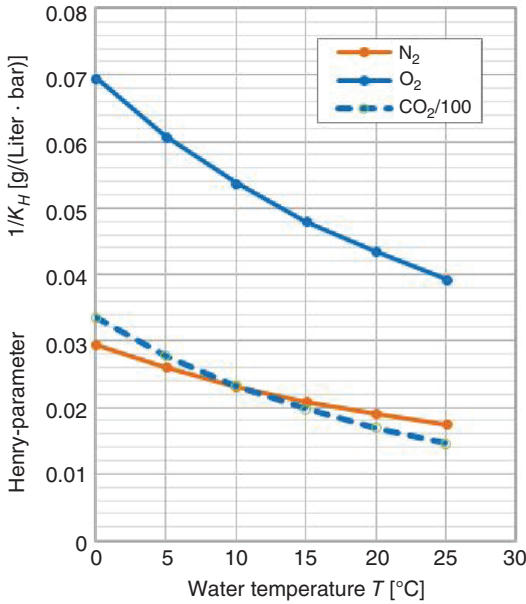


Figure 1.13 Temperature dependence of the Henry parameter $1/K_H$ of O_2 and N_2 , and $(1/K_H)/100$ for CO_2 , Values from W. Aeschbach-Hertig (Heidelberg University).

pressure p_i or total pressure. According to this

$$c_{W_i} = \frac{1}{K_{H_i}} \cdot p_i \quad [\text{g}/(\text{Liter} \cdot \text{bar})] \quad (1.45)$$

The Henry parameters K_H are determined experimentally. **Figure 1.13** gives for the three selected gases O_2 , N_2 and CO_2 the values of the factor $1/K_{H_i}$ as a function of temperature and a gas pressure of 1 bar. The correct value for CO_2 is the diagram value $\times 100$.

For oxygen, at a water temperature of 20°C , an atmospheric pressure of 1 bar and the partial pressure of 0.21 bar, the concentration of dissolved O_2 is as follows

$$c_{W_i} = 0.043 \cdot 0.21 = 0.00903 \quad [\text{g}/\text{liter}] = 9.03 \quad [\text{g}/\text{m}^3]$$

Assuming partial pressures of 21% for oxygen and 78% for nitrogen, the following concentration for air $c_{W_{air}}$ at 20°C is obtained (approximately) using the Henry values of the diagram:

$$c_{W_{air}} = (0.21 \cdot 0.043 + 0.78 \cdot 0.019) \cdot 1000 = 23.9 \quad [\text{g}/\text{m}^3]$$

The solubility of gases increases significantly with decreasing temperature, but especially with increasing total pressure. In 20 [m] water depth, for example, the solubility of nitrogen due to the pressure increased by 2 bar is instead of $14.8 \text{ [g}/\text{m}^3]$

$$c_{W(N_2)} = 0.019 \cdot (0.78 + 2.0) \cdot 1000 = 52.8 \quad [\text{g}/\text{m}^3]$$

In the presence of appreciable amounts of other ions or very saline waters, the soluble gas concentrations may deviate from the Henry values. Thermodynamic equilibrium calculations are then necessary.

1.3.7 Cavitation in the System Water/Vapor

In the context with the tensile stress of water in capillary pores, the problem area of cavitation in the water/vapor system will first be highlighted.

The phenomenon of cohesion loss due to cavitation (i.e. the spontaneous transition of water into vapor) can occur when a volume of water is subjected to tensile stress, especially when the water contains small vapor bubbles, for example, on external contact surfaces or impurities. **Cavitation can occur, for example, in free water at strong underpressure formation** $\ll p_{atm}$ in the area of fast-rotating ship propellers and lead there to propulsion loss in the long run to material damage, compare for example [26].

The danger of cavitation arises when the pressure in the water approaches the boiling point pressure corresponding to the given temperature. **From the phase diagram of water**, it can be seen that when the external pressure drops from $p_{atm} = 10^5$ [Pa] to 2340 [Pa], the water already boils at 20 °C and thus loses cohesion without active external tensile stress.

The influence of the negative pressure can also be seen in the so-called “geodesic suction head” for suction pumps, where water is pumped from depth by suction at the top. In this case, a maximum suction head is obtained by applying the Eq. (1.27) with $p_{cap} = p_{atm} = 1.013 \cdot 10^5$ [Pa] and $\rho_L \cdot g = 1000 \cdot 9.81 = 9810$ [Pa] to **$h = 10.33$ [m]**, at which the suction tension at the top corresponds to the atmospheric pressure and the cohesion of the water molecules fails there. The suction heights that can be realized in practice are significantly lower.

As a rule, the occurrence of cavitation is favored by impurities or water vapor bubbles. In this case, possible cohesion failure is closely **related to any vapor bubbles that may be present and to existing underpressure**. According to [27] or [26], a new formation or enlargement of vapor bubbles requires an amount of energy, which can be simply expressed with the fraction from the internal surface enlargement and the fraction of work to increase the volume of the bubble under the given pressure $p - p_{atm}$ as follows:

$$\Delta E = 4 \cdot \pi \cdot r^2 \cdot \gamma_L + \frac{4 \cdot \pi}{3} \cdot r^3 \cdot (p - p_{atm}) \quad (1.46)$$

Here, p is a tensile stress applied on the water surrounding the air bubble. This tensile stress is applied in addition to the atmospheric pressure p_{atm} (operating on all sides) and reduces the total pressure acting on the bubble or air pore.

Putting into the derivative the radius r of this equation equal to zero, we get the critical radius r^* depending on γ_L and $(p - p_{atm})$, at which the energy demand for bubble formation shows the maximum and is considered as “energy barrier.”

$$r^* = \frac{2 \cdot \gamma_L}{p_{atm} - p} \quad [\text{m}] \quad (1.47)$$

This result is also consistent with the following consideration of the equilibrium between the pressure within the bubble from surface tension and an imposed negative pressure p [Pa] in the surrounding water:

$$p_{atm} + \frac{2 \cdot \gamma_L}{r^*} = p + p_{atm} \Rightarrow p = \frac{2 \cdot \gamma_L}{r^*} \Rightarrow r^* = \frac{2 \cdot \gamma_L}{p} \quad (1.48)$$

Cohesion is abruptly lost when vapor bubbles larger than r^* in diameter are present. **In fine capillary pores, negative capillary pressures much larger than $-p_{atm}$ exist** and are therefore much larger than the “geodesic suction heights” previously calculated.

If the water has no impurities and no incipient vapor bubbles that cause heterogeneous nucleation, it can withstand high tensile forces in the “undisturbed state” in laboratory experiments up to the magnitude order of several 100 bar until cohesion failure [26].

1.4 Sorptive Storage on Material Surfaces and on the Inner Surface of Pore Systems

1.4.1 Preliminaries

The saturation of surface free energy on solid surfaces by gas molecules, especially water vapor molecules from air, and the sorption of molecules in contact with liquids, have long been the subject of research. The sorption behavior is usually described by sorption isotherms based on empirical or thermodynamic methods. As is well known, a distinction must be made between chemical and physical sorption.

The following remarks concentrate on the important area of physical sorption, in particular also for internal surfaces, and on the consequences for the “water balance” of the material in the case of water vapor sorption.

The sorption isotherms measurable in physical sorption give the relationship between the ambient gas pressure, for example, the water vapor partial pressure, and the mass of gas molecules V_{ads} bound to the surface under consideration as a liquid layer in equilibrium with the external partial pressure p_0 .

Groups of adsorption forces, which are based on polar effects or on dispersion forces or Van der Waals forces, are responsible for the physisorption. The recorded atomic or molecular distances are ≈ 0.2 to ≈ 10 [nm]. A large number of researchers have dealt with this. Reference is made to Israelachvili [28], Rouquerol et al. [29], and Lauth and Kowalczyk [19].

In Figure 1.14 are shown the names for the processes and the phases as they are encountered in physisorption of most gases or vapors on nonporous or macro-porous materials.

For the calculation resp. prediction of the mentioned physical adsorption mechanisms, there are a number of models resp. approaches that consider interactions between molecules in different ways and model a mono-molecular to multi-molecular coverage of the surface, compare [19]. These methods allow the prediction of adsorption on pore-free surfaces and on internal surfaces of porous solids **up to relative gas pressures or relative vapor pressures of about 0.40**. Adolphs and Setzer [30] shows a comparison of the ability of a number of the models to simulate the sorption measurement results of N_2 on SiO_2 powder.

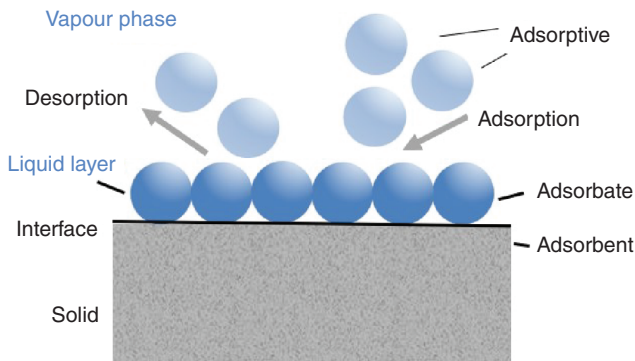


Figure 1.14 Vapor molecule physisorption on solid surfaces. Designations of the phases and components.

The most common of these methods is the BET method of Brunauer/Emmett/Teller-1938 [31]. This can be used to reliably determine the monolayer capacity and total internal surface area. The BET method will be discussed in more detail below.

Another approach to describing sorption isotherms can be based on thermodynamic derivatives, as shown by Adolphs and Setzer [30] and Badmann et al. [32]. Further discussion of this is also given below.

A new approach to the description of adsorption isotherms has been worked out by Zandavi and Ward [33] and Zandavi [34]. They assume (actually existing) cluster formation of vapors of different adsorptive, increasing covering densities as well as chemical potential of clusters of different sizes. The physical parameters required for the theory, however, must be determined from sorption measurements, but are then valid for the entire partial pressure course of the isotherms and can also be led beyond $\varphi = 1.0$ to a certain extent.

1.4.2 Measured Surface Sorption of Water Vapor on Flat Nonporous Surfaces

Sorption isotherms measured on porous mineral materials contain increasing amounts of water from capillary condensation with increasing relative humidity. For a more detailed analysis of sorption processes and possible thermodynamic calculations, however, it is necessary to know the condensate layer thicknesses developing with increasing gas partial pressure **on pore-free surfaces**, especially when approaching saturation partial pressure.

Measurement results from different authors are available for this purpose. The sorption layer thicknesses are determined with the aid of gravimetric fine measurements, in particular TGA measurements, and are usually presented as a mathematical function between layer thickness and relative partial pressure or the relative humidity in the case of water vapor sorption measurements.

Reference is made, for example, to **Badmann et al. [32]**. This reports on water vapor sorption measurements on cement phases and samples from hydrated cements of different compositions and different water–cement ratios. The functional

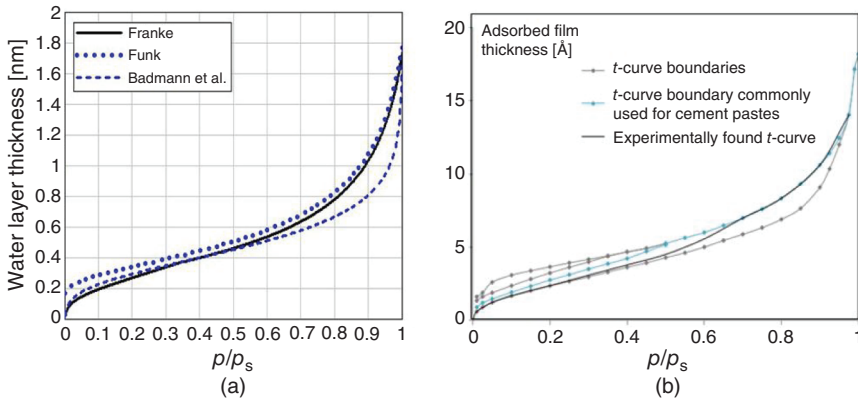


Figure 1.15 Sorption isotherms for water vapor with pore-free surface. (a) From Franke, Eq. (1.50). (b) Source: From Snoeck et al. [37]/with permission of Elsevier.

dependence of the averaged values for water vapor sorption is given as:

$$t(\varphi) = 0.385 - 0.189 \cdot \ln(-\ln(\varphi)) \quad [\text{nm}] \quad (1.49)$$

Funk [35] compares $t(\varphi)$ -curves of different authors and recommends the function dependence of deBoer et al. [36]. **These curves are plotted in Figure 1.15a** together with a curve of [Franke]. The comparative calculations made by Franke with sorption isotherms lead to a slightly modified dependence of the sorption layer thicknesses and to the proposal of the following function. **Figure 1.15b** shows measurement results from Snoeck et al. 2014 [37] with a curve shape very close to the curve proposal from Franke (Eq. (1.50)):

$$t(\varphi) = \varphi^{0.028} - 1.03 + \left(\frac{0.09}{\log\left(\frac{1}{\varphi}\right) + 0.03} \right)^{0.5} \quad [\text{nm}] \quad (\varphi \geq 0.0115) \quad (1.50)$$

With this function, the monolayer is obtained with $t = 0.30$ [nm] at $\varphi(n_{mono}) = 0.23$ and $t = 1.70$ [nm] at the saturation partial pressure.

In Section 1.4.6.1, we investigate to what extent the basic isotherm for nonporous (hydrophilic) surfaces derived here on the basis of experimental results can also be approximated theoretically on the basis of thermodynamic approaches. In addition, Section 1.4.6 considers issues relating to sorption film formation within material pores as well as on differently curved surfaces.

1.4.3 Use of Water Vapor Sorption Isotherms to Determine the Value of the Internal Surface Area

Knowledge of the **internal surface area of porous material**, particularly cement-bound products, is important for moisture storage and transport considerations. Typically, sorption experiments with nitrogen N_2 or helium H_2 are performed

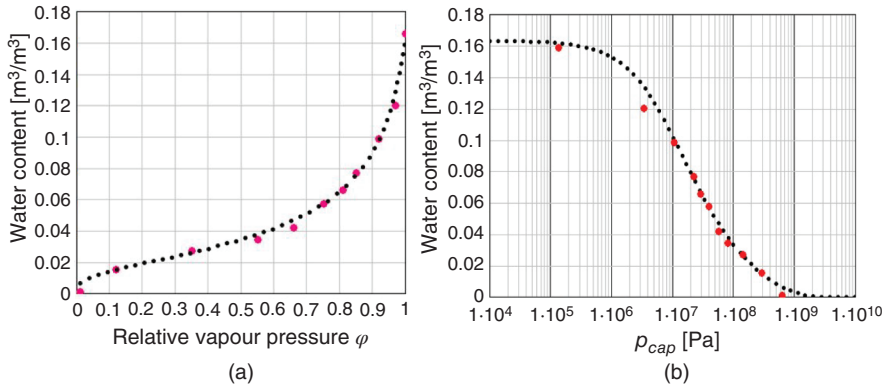


Figure 1.16 (a) Measured points and regression curve of the adsorption isotherm of material REF ($W/C = 0.45$). (b) Isotherm of the material REF, related to the capillary pressure p_{cap} .

to determine these. **It will be shown that the inner surface can be determined with the known evaluation methods on the basis of existing water vapor sorption isotherms.** This is shown below by means of an example based on the BET method and the method of Adolphs and Setzer. **Figure 1.16a** shows the adsorption isotherm of the reference material REF mainly used in experiments in the present project. The function of the measured adsorption isotherm is given by Eq. (1.51). **Figure 1.16b** shows the adsorption isotherm as a function of capillary pressure p_{cap} for comparison. This capillary pressure dependent isotherm or moisture storage function is obtained by converting the output function (1.51) of **Figure 1.16a** using the Eq. (1.1).

1.4.3.1 Total Internal Surface Determined Using BET Method

To determine the internal surface area of the Portland cement on reference mortar REF, the BET method is used.

The derivation of the equations to be used can be taken in detail from Brunauer et al. [31], Rouquerol et al. [29], and, in particular, Lauth and Kowalczyk [19]. The BET method is capable of simulating coverage with multiple layers of the respective gas molecules, in this case, water vapor molecules. However, previous experience shows that if a partial vapor pressure of about 0.40 is exceeded, an overestimation of the sorbed liquid quantity occurs, so that an **application of the BET method should only be made in the partial pressure range of about 0.05 to 0.4.**

In the following example, the starting point of the evaluation is the sorption isotherm already shown in **Figure 1.16a.**

The aim of the evaluation is first to determine the so-called monolayer capacity in order to derive from it the inner surface area using the example of the REF material mainly used in our experiments.

Equation (1.51) is the equation of the adsorption isotherm or moisture storage function in [m³/m³] for the REF material. Indicated are the coefficients $A, a, b,$

and c to be used. The inverse function $\varphi_\theta(\theta)$ is given as Eq. (1.52) with the same coefficients.

$$\theta\varphi(\varphi) = a \cdot \frac{1}{\left[\left(\frac{A}{\varphi}\right)^c - 1\right]^{\frac{1}{b}}} \quad (1.51)$$

$$A = 1.065 \quad a = 0.0197 \quad b = 1.70 \quad c = 0.43$$

$$\varphi_\theta(\theta) = A \cdot \left[\left(\frac{a}{\theta} + 1\right)^b\right]^{\frac{-1}{c}} \quad (1.52)$$

The Eq. (1.53) is the well-known basic equation of the BET method, derived or explained in the previously given publications. By varying the parameter C , the course of the curve can be adapted to given sorption measurement results. **Figure 1.17** shows the resulting curves for parameters 1–100 as a function of the gas partial pressure. One can see the good adaptability to different measurement results.

$$\frac{n}{n_{mono}} = \frac{C \cdot \varphi}{(1 - \varphi) \cdot (1 - \varphi + C \cdot \varphi)} \quad (1.53)$$

The basic Eq. (1.53) can be transformed into the well-known linear form $y(\varphi) = a + b \cdot \varphi$ of the Eq. (1.54) as a function of φ . In the left part of the equation, n corresponds to the sorbed liquid amount, n_{mono} in the right side of the equation corresponds to the monolayer capacity. The left part of the Eq. (1.54) is given as $y_0(\varphi)$ with the measurement results of the moisture storage function (1.51) as Eq. (1.55)

$$\frac{\varphi}{n \cdot (1 - \varphi)} = \frac{1}{C \cdot n_{mono}} + \frac{(C - 1)}{C \cdot n_{mono}} \cdot \varphi \quad (1.54)$$

$$y_0(\varphi) = \frac{\varphi}{\theta\varphi(\varphi) \cdot (1 - \varphi)} \quad (1.55)$$

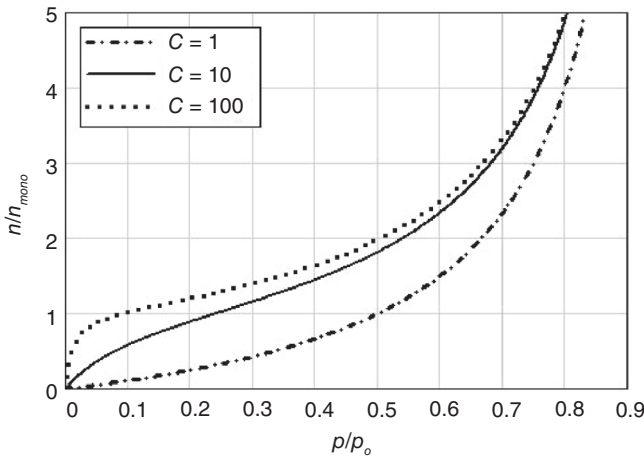


Figure 1.17 BET sorption curves according to Eq. (1.53) as a function of parameter C .

It is generally assumed that the BET Eq. (1.53) is valid up to a relative partial pressure of about 0.40 for surfaces. At higher partial pressures, the process results in overemphasized adsorption.

From the measured value curve resp. sorption isotherms $\theta\varphi(\varphi)$, now two points $\varphi_1/y_0(\varphi_1)$ and $\varphi_2/y_0(\varphi_2)$ are taken in the mentioned partial pressure range to determine the axis intercept $y_{00}(\varphi_1, \varphi_2)$ of the straight line $y_0(\varphi)$. The following values were used:

$$\varphi_1 = 0.15 \quad y_0(\varphi_1) = 10.56 \quad \varphi_2 = 0.35 \quad y_0(\varphi_2) = 20.51$$

$y_{00}(\varphi_1, \varphi_2)$ results from

$$y_{00}(\varphi_1, \varphi_2) = y_0(\varphi_2) - \frac{y_0(\varphi_2) - y_0(\varphi_1)}{\varphi_2 - \varphi_1} \cdot \varphi_2 \quad (1.56)$$

From Eq. (1.57), the coefficient b is obtained as the slope of the straight line Eq. (1.54). Using the intercept y_{00} , the curve parameter C is then obtained from Eq. (1.58).

$$b = \frac{y_0(\varphi_2) - y_0(\varphi_1)}{\varphi_2 - \varphi_1} \quad (1.57)$$

$$C = \frac{b}{y_{00}(\varphi_1, \varphi_2)} + 1 \quad (1.58)$$

For the REF material (resp. the curve in Figure 1.16a corresponding to the black curve in Figure 1.19) the following values are obtained:

$$y_{00}(\varphi_1, \varphi_2) = 3.1 \quad b = 49.74 \quad C = 17.0.$$

With C known, n_{mono} is obtained from Eq. (1.59):

$$n_{mono} = \frac{1}{C \cdot y_{00}(\varphi_1, \varphi_2)} \quad (1.59)$$

For the REF material, $n_{mono} = 0.019 \text{ [m}^3/\text{m}^3\text{]}$. The inner surface area A_{BET} we are looking for follows from Eq. (1.60):

$$A_{BET} = \frac{n_{mono} \cdot N_A \cdot A_{molecule}}{n_{mol}} \quad (1.60)$$

with the Avogadro number $N_A = 6.022 \cdot 10^{23}$, the molar volume for water n_{mol} , and the area occupied by a water molecule (according, for example, to [38]) $A_{molecule} = 11.4 \cdot 10^{-20}$. For the REF material under consideration, the inner surface area of the REF material we are looking for amounts to:

$$A_{BET} = 7.24 \cdot 10^7 \text{ [m}^2/\text{m}^3\text{]} = 72.4 \text{ [m}^2/\text{cm}^3\text{]} \quad \varphi_\theta(n_{mono}) = 0.20$$

In Figure 1.18, the resulting curves n/n_{mono} according to Eq. (1.53) and the REF sorption isotherm divided by the value n_{mono} (red curve) are compared. Very good agreement is seen, generally up to a relative partial pressure of about 0.40.

For comparison, the inner surface A_{BET} of the red curve in Figure 1.19 was also determined according to the steps shown previously. The following values were obtained, from which one can see the suitability resp. precision of the BET method:

$$C = 9.1 \quad n_{mono} = 0.020 \quad \varphi_{mono} = 0.25 \quad A_{BET} = 76.4 \text{ [m}^2/\text{cm}^3\text{]}$$

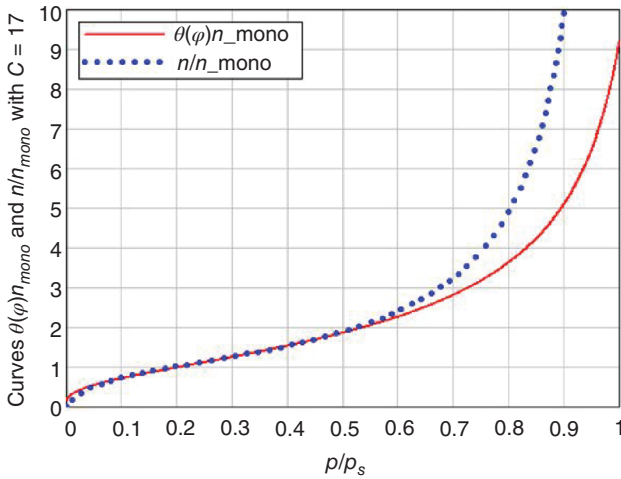


Figure 1.18 Comparison of the BET modeled sorption curve according to Eq. (1.53) with $C = 17.0$ (blue) and the measured n_{mono} related basic (red) curve from REF isotherm (curve **Figure 1.16a** or the black dotted curve in **Figure 1.19**).

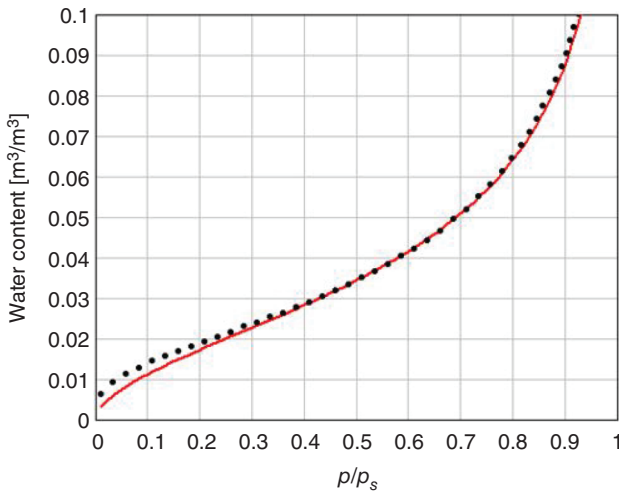


Figure 1.19 Sorption isotherm for the REF material according to **Figure 1.16a** (black dotted) and sorption isotherm (red) with slightly lower water absorption up to $p/p_s = 0.40$ with respect to a computational comparison of the monolayer capacity.

In their 1969 publication [39], Brunauer et al. propose an extension of their BET method in which the vapor partial pressure is multiplied by a factor $k < 1.0$ in the linear basis Eq. (1.54). This can be used to extend the agreement to measured values beyond the relative partial pressure of about 0.40. Pavlik et al. [40] apply the modified procedure to comparative modeling of sorption isotherms of different building materials and find improved agreement. As a criticism, there is no physical justification for the extended BET method, and thus this extended

equation is merely an empirical equation for modeling sorption isotherms, see also Rouquerol/Sing [29]/section 5. In contrast, the classical BET method is sufficient for determining the internal surface area of materials.

1.4.3.2 Total Internal Surface Determined by the Method of Adolphs and Setzer

The Adolphs/Setzer method for determining the internal surface area of a porous material is described in Adolphs/Setzer [30, 41], and [42]. It can be applied to different gases and different material surfaces.

The following shows what results are obtained with respect to the internal surface area when water vapor sorption isotherms are used for its determination. This also results in a comparison to the BET method.

Adolphs/Setzer assume the following equation:

$$\Phi = n_{ads} \cdot \Delta\mu \quad (1.61)$$

Φ is used to describe a change in surface free energy upon sorption of gas molecules, here specifically water vapor. Φ is defined by Adolphs/Setzer as “**Excess surface work.**” In Eq. (1.61), n_{ads} is the sorbed liquid mass, and $\Delta\mu$ is the change in chemical potential corresponding to Eq. (1.62).

$$\Delta\mu = RT \cdot \ln \left(\frac{p}{p_s} \right) \quad [\text{J/mol}] \quad (1.62)$$

After introducing the sorbed water of sorption isotherms $\theta\varphi(\varphi)$, the corresponding excess surface work equation follows from Eq. (1.61).

$$\Phi(\varphi) = RT \cdot \ln(\varphi) \cdot \theta\varphi(\varphi) \quad (1.63)$$

According to the method of Adolphs/Setzer, the low point of the curve 1.63 corresponds to the value n_{mono} resp. θ_{mono} .

Accordingly, if we first evaluate the red curve of **Figure 1.20** with respect to the (red) sorption isotherm of **Figure 1.19**, we obtain for $T = 293.15$ the following values:

$$\theta_{mono} = 0.020 \quad \varphi_{\theta}(\theta_{mono}) = 0.219$$

These results agree well with the values determined after BET procedure.

From Eq. (1.62), we get then with θ_{mono} the relation for $\Delta\mu_0$:

$$\Delta\mu_0 = RT \cdot |\ln(\varphi_{\theta}(\theta_{mono}))| \quad (1.64)$$

The remarks of Adolphs/Setzer show that $nn(\varphi_{\theta}) = n_{ads}/n_{mono}$ lead to Eq. (1.65).

$$nn(\varphi_{\theta}) = 1 - \ln \left[\frac{RT \cdot |\ln(\varphi_{\theta})|}{\Delta\mu_0} \right] \quad (1.65)$$

From (1.65), $nn(\varphi_{\theta}) = 1$ can be used to derive the value for $\Delta\mu_0$ resp. Eq. (1.64). Substituting the previously calculated value $\varphi_{\theta}(\theta_{mono}) = 0.219$, we obtain the following values:

$$nn = n_{ads}/n_{mono} \quad \Delta\mu_0 = -3.703 \cdot 10^3 \quad nn(\varphi_{\theta}(\theta_{mono})) = 1$$

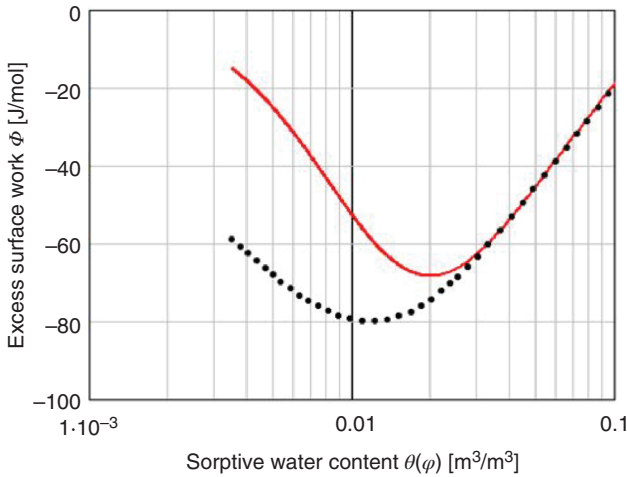


Figure 1.20 Excess surface work curves according to Eq. (1.63) for the adsorption isotherms according to **Figure 1.19**. The low points give the values for n_{mono} and θ_{mono} , respectively.

If, on the other hand, the same calculation is performed for the (black dotted) sorption isotherm according to **Figure 1.19** with its equation $\varphi_{\theta}(\theta)$ according to Eq. (1.52), the following values result with the black dotted determination curve according to **Figure 1.20**:

$$\theta_{mono} = 0.013 \quad \varphi_{\theta}(\theta_{mono}) = 0.081.$$

The corresponding internal surface area for this according to Eq. (1.60) is $A_{Adolphs} = 49.6 \text{ [m}^2/\text{cm}^3]$ and is thus significantly lower than the reference value $A_{BET} = 72.2 \text{ [m}^2/\text{cm}^3]$ according to BET.

The data of other authors on the internal surface area of mortar products similar to the material considered here amounts to at least $30 \text{ [m}^2/\text{g}]$ corresponding to at least approx. $65 \text{ [m}^2/\text{cm}^3]$, so that the calculated approx. $50 \text{ [m}^2/\text{cm}^3]$ appears too low. The reason for this would require a more detailed analysis.

Figure 1.21 shows the comparison of the resulting curve $nn(\varphi_{\theta})$ and the associated sorption isotherms related to n_{mono} . Agreement between the curves is obtained up to a partial pressure of about 0.25.

1.4.4 Calculation of the Pore Size-Dependent Distribution of the Inner Surface Using the Moisture Storage Function

Although the relationships and results presented below are specific to the reference REF material, they are applicable to other porous materials with known moisture storage functions. The explanations show the calculation of the course of the inner surface as a function of the relative partial pressure or the pore-radius distribution, which is also calculated, using the moisture storage function resp. the adsorption isotherm as a starting point.

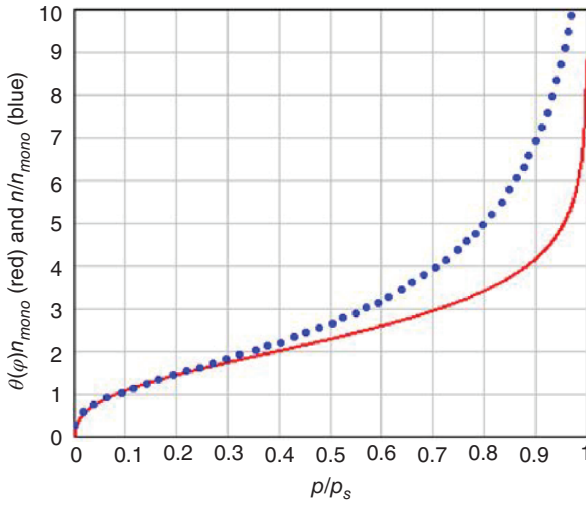


Figure 1.21 Comparison of the curve $nn(\varphi_\theta)$ calculated according to Adolphs/Setzer with the sorption isotherms related to n_{mono} .

Furthermore, the distribution of the different moisture fractions surface sorbate and capillary condensate are also calculated in dependence of the relative partial pressure.

1.4.4.1 Determination of the Net Sorptive Storage Function

Figure 1.22 schematically shows that the original sorptive isotherm resp. moisture storage function, for example, of the material REF in **Figure 1.16a** is not very suitable for a more accurate determination of the pore size distribution or for the determination of the course of the inner surface. This is because the function value $\theta_{Isoth(\varphi_1)}$ associated with a φ_1 has not only the content of condensed water at φ_1 , but additionally the water adsorbed on the inner surface of the pores in the not yet

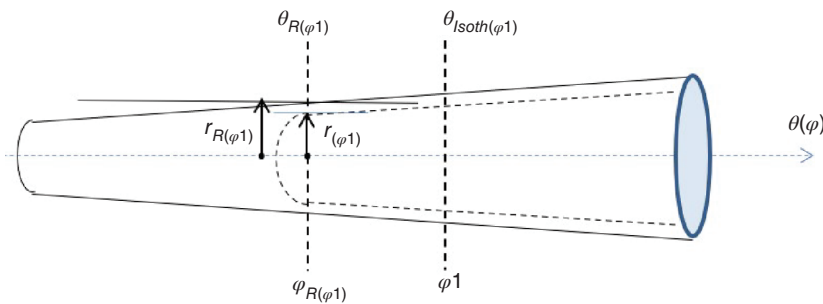


Figure 1.22 Schematic representation of a cylindrical pore with increasing radius as well as the meniscus associated with a selected relative partial pressure φ_1 and the associated surface film of thickness $t(\varphi_1)$ in the non-water-filled pore region.

filled region before a meniscus. Therefore, the curve without the sorbed fraction must be determined first.

The determination of this “**net storage function**” can be done by first calculating the pore-size distribution from the original isotherms as shown below, and then using the sorbed surface fraction to calculate the net storage function we are looking for. This procedure is described in further detail below in Section 1.4.6.3. First, an approximate equation is used. Comparison calculations show that the following Eq. (1.66) gives the net storage function with a very good approximation:

$$\theta\varphi_N(\varphi) = \theta\varphi(\varphi) \cdot \varphi^{0.5} \quad (1.66)$$

The net storage function is given in **Figure 1.23a** as a function of $\varphi = p/p_S$ as a line $\theta\varphi_N(\varphi)$. In addition, the “exact” curve $[\theta(\varphi) - \Delta Wh(\varphi)]$ is given, resulting from the calculation of the internal surface area and vapor sorption curve still shown below. There is very good agreement between these curves of the net storage function.

In **Figure 1.23b**, the required curves are given as a function of r and the pore radius r_R . The reference curve $\theta r(r)$ is calculated with the (here abbreviated) Kelvin equation (1.67) plus (1.68) from $\theta\varphi(\varphi(r))$.

$$\varphi(r) = \exp\left(\frac{M_\gamma}{r}\right) \quad (1.67)$$

$$M_\gamma = -\frac{\bar{V}_L \cdot 2 \cdot \gamma_L \cdot \cos(\theta)}{R \cdot T} \quad (1.68)$$

However, in order to determine realistic progressions of the inner surface on the basis of the net storage function, not a dependence on the mean pore radius r should be used, but the dependence on the “real” mean pore radius $r_R = r(\varphi) + t(\varphi) \cdot 10^{-9}$.

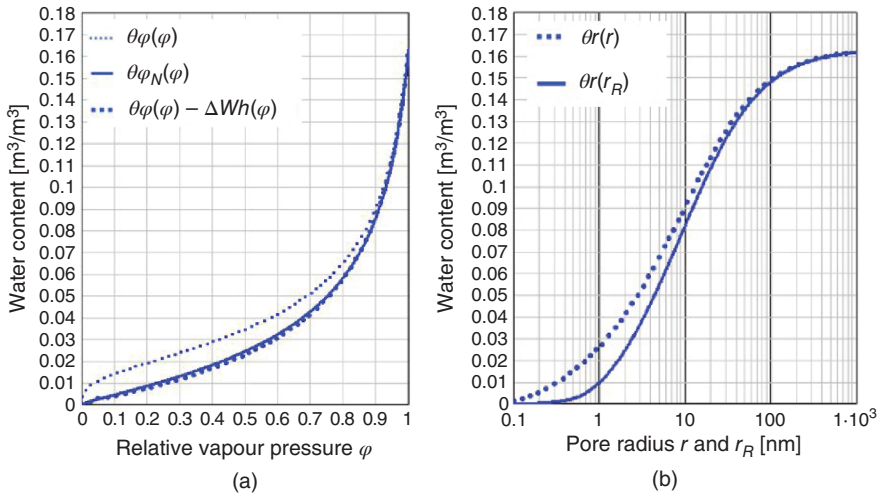


Figure 1.23 Measured sorption isotherm $\theta\varphi(\varphi)$ of the sample material REF and its accurate formulation $\theta\varphi(\varphi) - \Delta Wh(\varphi)$, furthermore the net storage functions $\theta r_{R,N}(r_R)$ ($= \theta r(r_R)$ in figure (b)) calculated from Eq. (1.66). (a) Relative to vapor partial pressure. (b) Relative to the effective “real” pore radius r_R .

This net storage function, which depends on the effective radius, is plotted in **Figure 1.23b** as $\theta_{r_{R,N}}(r_R)$.

The net storage function calculated on the basis of the internal surface area via vapor sorption is obtained from Eq. (1.89), also shown in **Figures 1.23a and 1.32**.

1.4.4.2 Basic Equation for the Pore Size-Dependent Distribution of the Inner Surface

For a given radius r_R , the net storage function exhibits the volume increase $d\theta(r_R)/dr_R$. The volume of associated pores with largely unknown pore shapes can be generally formulated as $k_V \cdot r_R^3$, the associated internal surface area of these pores as $k_A \cdot r_R^2$.

The associated internal surface area increment is then equal to the theoretical number of pores of radius r_R in the pore area dr_R , to be calculated from the associated volume increment divided by the formulated pore volume $k_V \cdot r_R^3$.

The associated surface area increment is then obtained by multiplying the pore number by its assumed internal surface area $k_A \cdot r_R^2$.

The inner surface area of the pore system between two radii r_{R1} and r_{R2} is then obtained from the net storage function to

$$A(r_{R1}, r_{R2}) = \int_{r_{R1}}^{r_{R2}} \frac{d\theta_{r_{R,N}}(r_R)}{dr_R} \cdot \frac{k_A \cdot r_R^2}{k_V \cdot r_R^3} \cdot dr_R \quad (1.69)$$

Of importance now is the question of the pore shape factors to be applied, which can be combined into a common pore shape factor $k_p = k_A/k_V$.

For cylindrical pores, $A/V = 2/r$, i.e. $k_p = 2$, for conical from wide to narrow pores, A/V would be $\approx 1.01/r$, for spherical pores $A/V = 3/r$. Ridgway et al. [43], in modeling pore-size distributions, shows that by incorporating conical pore shapes, a better fit to “natural” pore progressions is obtained. Hereafter, $k_p = 2$ is used as the initial value (the applicable value is determined in Section 1.4.4.4). **Equation (1.69) is then the basic equation for the internal surface area curve for the region between two pore radii r_{R1} and r_{R2} assuming a largely matching pore structure in the volume region between these two pore radii.**

$$A(r_{R1}, r_{R2}) = \int_{r_{R1}}^{r_{R2}} \frac{d\theta_{r_{R,N}}(r_R)}{dr_R} \cdot \frac{1}{r_R} \cdot k_p \cdot dr_R \quad (1.70)$$

1.4.4.3 Application of the Basic Equations with Regard to the Material REF

Application of the basic equation for the calculation of the course of the internal surface specific calculations of the course of the internal surface of a material based on the net storage function with the integral (1.70) require the specification of the lower and upper limits for the area calculation. If the calculation of the total internal surface area is desired, the approximated water molecule diameter should be used as the lower bound for water as the initial radius, i.e. $r_R = 0.30 \cdot 10^{-9}$ [m]. As end radius or upper limit it is convenient to use the upper limit radius of the mercury

porosimeter MIP, in the present case $1.50 \cdot 10^{-4}$ [m]. Since the area increment in the region of the upper radius of the pore system is relatively low for materials such as the REF used here as the sample material, the error is small if, for example, $1.50 \cdot 10^{-5}$ [m] is used instead. **The area calculation started from the lower boundary is then with variable upper boundary radius:**

$$A(r_{R1}) = \frac{1}{10^6} \int_{0.30 \cdot 10^{-9}}^{r_{R1}} \frac{d\theta_{r_{R-N}}(r_R)}{dr_R} \cdot \frac{1}{r_R} \cdot kp \cdot dr_R \quad (1.71)$$

For the upper limit $r_{R1} = 1.50 \cdot 10^{-5}$ [m], the pore shape factor $k_p = 2$ gives a total area for the pattern material REF of $A(1.50 \cdot 10^{-5}) = 109.7$ [m²/cm³]. The factor $1/10^6$ in front of the integral gives the conversion to [m²/cm³].

Including a bulk density of the REF material of 2.10 [g/cm³], this basic calculation yields a total internal surface area of $A_i = 52.2$ [m²/g].

An alternative calculation can be made by entering the boundaries as a function of relative air humidity φ . The integral for the course of the inner surface from any lower limit $r_R(\varphi_1)$ to the upper limit for example $\varphi \approx 1.0$ is then

$$A(\varphi_1) = \frac{1}{10^6} \cdot \int_{r_R(\varphi_1)}^{r_R(0.99999)} \frac{d\theta_{r_{R-N}}(r_R)}{dr_R} \cdot \frac{1}{r_R} \cdot kp \cdot dr_R \quad [\text{m}^2/\text{cm}^3] \quad (1.72)$$

If $r_R(\varphi_1) = 0.30 \cdot 10^{-9}$ [m] is to be used as lower integration limit, as before in Eq. (1.71), the corresponding φ_1 value must be chosen for this start value with the help of Eq. (1.80) in such a way that $0.30 \cdot 10^{-9}$ [m] results from it. This value is $\varphi_1 = 0.0116$, as the result of the following equation (with $t(\varphi)$ from Eq. (1.50)) shows

$$r_{R(\varphi_1=0.0116)} = r(0.0116) + t(0.0116) \cdot 10^{-9} = 3.00 \cdot 10^{-10}$$

If one chooses instead approximately $\varphi_1(r = 0.30 \cdot 10^{-9}) = 0.031$ according to the standard Kelvin equation and from this the starting radius $r_R(\varphi_1 = 0.031) = 0.42 \cdot 10^{-9}$ [m], the Eq. (1.72) now yields the area 102.1 [m²/cm³] instead of the correct value 109.7 [m²/cm³].

1.4.4.4 Calibration of the Pore Shape Parameter and Calculation of the Internal Surface Distribution of the Material REF

In the previously commented basic integrals for the calculation of the course of the inner surface, the pore-shape factor $kp = 2$ of a cylindrical pore structure was used. However, the other theoretical pore shape factors given show that for realistic modeling, pore shape factor 2 is unlikely to be suitable for materials such as the REF material. It therefore suggests itself to look for a calibration possibility. A calibration based on MIP measurement results would be conceivable, but preferably based on the total internal surface area determined according to BET, as shown below.

The pore shape parameter kp is adjusted to k_N such that the surface integration yields the total internal surface area A_{BET} of the pore system as

determined by the BET method :

$$k_N = kp \cdot \frac{A_{BET}}{A(r_{R1}, kp = 2)} = 2.0 \cdot \frac{72.4}{109.7} = 1.32 \tag{1.73}$$

With $k_N = 1.32$ and the lower limit $r_R(\varphi_1 = 0.0116)$, the Eq. (1.72) now gives a total inner area of 72.4 [m²/cm³]. With $k_N = 1.32$, also the Eq. (1.71) yields this **total internal area related to 1 [g] corresponding to $A_i = 34.5$ [m²/g]**.

It was also tested whether a calibration of the pore structure parameter was possible via the results of mercury intrusion porosimetry (MIP) measurements also leads to the target. The measuring range of the mercury porosimeter MIP used is $1.8 \cdot 10^{-9}$ to $1.51 \cdot 10^{-4}$. However, the internal surface area calculated by the porosimeter for this measurement range scatters between 8.5 and 12.5 [m²/g] for the material REF, for example, in successive manufacturing series despite strict manufacturing quality control and little scattering of other properties.

The integration with Eq. (1.71) over the pore measurement range of of the MIP based on a mean MIP measurement result of 10.0 [m²/g] leads after a k_{MIP} -determination analogously to Eq. (1.73) to the lower lines in **Figure 1.24a,b**, which do not satisfactorily represent the surface progression.

It should be noted that the pore shape parameter is used for the entire inner surface. However, the calculations for sorptive moisture storage subsequently based on this type of surface calculation yield satisfactory and comprehensible results. A further refinement of the modeling of the course of the inner surface could be achieved by adjusting the pore shape parameter section by section.

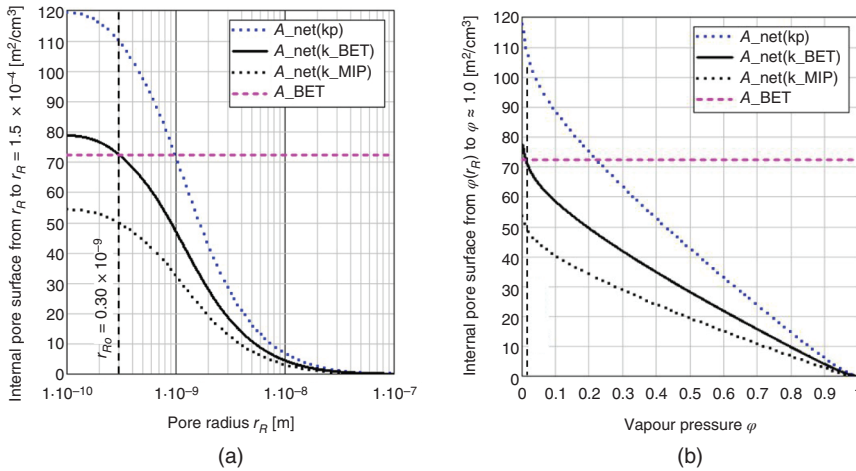


Figure 1.24 Course of the inner surface of the reference material REF above a given “real” pore radius r_R calculated via the net storage function with Eq. (1.71) as well as depending on the vapor partial pressure φ calculated with Eq. (1.72). The initial lines $A_{net}(kp)$ shown were obtained with the area shape factors $kp = 2$, and the optimized lines $A_{net}(k_{BET})$ with the shape facto k_N and k_{BET} , respectively. Attempting calibration based on the MIP measurement results leads to the inapplicable lines $A_{net}(k_{MIP})$. (a) $A_{internal}$ between r_R and $r_R \geq 10^{-7}$. (b) $A_{internal}$ between φ and $\varphi \approx 1.0$.

For this purpose, an additional evaluation of adsorption isotherms of representative material compositions would be necessary, for example, for cement paste with a low W/C value with regard to the gel-pore structure and the possibly deviating pore-structure parameter.

1.4.4.5 Distribution of the Volume of the Internal Adsorbed Water Films

The results presented in Sections 1.4.2 to 1.4.4 on the sorption of water vapor or water molecules, especially on the inner surface of the pores of porous materials, as well as the knowledge of the course of their inner surface, now allow to obtain quantitative results on details of moisture storage, i.e. on the proportional extent of sorption and condensation.

Volume fractions of the moisture storage function from surface sorption can be determined as a function of relative air humidity φ or pore radius $r_R(\varphi)$ by multiplying inner surface area by the corresponding adsorption layer thickness. Note that **film thicknesses occupy a smaller volume** $\Delta V(\varphi r)$ than on the same planar surface $\Delta V(\varphi)$ for a given film thickness $t(\varphi)$, by a factor $k_h(\varphi)$, the value of which can range from 0.5 to 1.0, due to curvature on the inner surfaces. From this follows the adsorbed volume:

$$\Delta V(\varphi) = \Delta A(\varphi) \cdot t(\varphi) \cdot k_h(\varphi) \quad (1.74)$$

Depending on the mean net pore radius $r_R(\varphi)$ and the corresponding film thickness $t(\varphi)$ (film thickness in [m] $\leq 0.5 \cdot r_R(\varphi)$), $k_h(\varphi)$ can be estimated to

$$k_h(\varphi) = 1 - \frac{t(\varphi)}{2 \cdot r_R(\varphi)} \quad (1.75)$$

The previously determined pore shape parameter k_N **states that the mean pore shape deviates significantly from a cylindrical shape**. $k_h(\varphi)$ can be additionally adjusted by considering the pore shape parameter k_N .

$k_h(\varphi)$ is then more generally given by $t(\varphi)$ in [m]:

$$k_{1h}(\varphi) = \frac{1}{1 + (k_N - 1) \cdot \frac{t(\varphi)}{r_R(\varphi)}} \quad (1.76)$$

When the ratio of the film thickness to the respective pore radius is low or for **flat surfaces** $k_{1h}(\varphi)$ **takes the value 1**, when the film thickness reaches the pore radius, the value of $1/k_N$.

Based on the Eq. (1.72), which calculates a fraction of the internal surface area between a chosen φ_1 and $\varphi = 1.0$, the **following Eq. (1.77) is obtained to determine a stored moisture volume resulting from a condensate film of constant thickness $t(\varphi_1)$ in [m] on the internal surface area captured by the integral**, which is bounded by the two chosen pore radii $r_R(\varphi_1)$ and $r_R(\varphi_2)$ (as lower and upper integration limits).

$k_{1h}(\varphi)$ within the integral accounts for the curvature influence from Eq. (1.76) of the inner surface. The included radius r_R is variable within the integral and must not be made dependent on φ_1 there, while $t(\varphi_1)$ is constant here according to the value before the integral. $t(\varphi_1)$ (if necessary from Eq. (1.50) must be entered in [m].

k_N is the pore shape factor calibrated for the considered material via BET.

$$\Delta V(\varphi 1) = t(\varphi 1) \cdot \int_{r_R(\varphi 1)}^{r_R(\varphi 2)} \frac{d\theta r_{R,N}(r_R)}{dr_R} \cdot \frac{1}{r_R} \cdot k_N \cdot k_{1h}(\varphi 1) \cdot dr_R \quad [\text{m}^3/\text{m}^3] \quad (1.77)$$

1.4.5 Equations for Capillary Condensation Considering Adsorbed Liquid Films

In Section 1.3.2, the mechanism of capillary condensation was described, and it was shown how the famous Kelvin equations (1.37) and (1.38), respectively, can be determined. If one now determines the associated mean pore radius for a given external relative air humidity or, conversely, the associated air humidity from a given pore radius, one commits an error, at least formally, due to the fact that the meniscus radius is reduced by the liquid layer sorbed on the inner surface, and this results in a relative air humidity that is smaller than that belonging to the real pore radius, see **Figure 1.25a**.

Therefore, the Eqs. (1.37) and (1.38) are to be expanded with the local film thickness to the “real” pore radius r_R

$$r_R(\varphi) = r(\varphi) + t(\varphi) \quad (1.78)$$

with r = Kelvin radius and $t(\varphi)$ = film thickness in [m].

Alternatively, Eq. (1.78) can be expressed by the following equation:

$$r_R(\varphi) = \frac{M_\gamma}{\ln(\varphi)} + t(\varphi) \quad \text{in [m]} \quad (1.79)$$

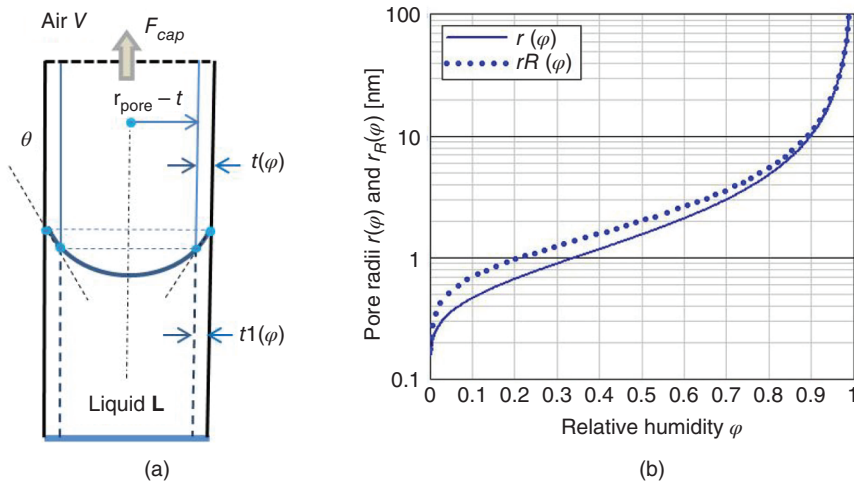


Figure 1.25 (a) Cylindrical capillary pore with meniscus and sorbed layer thicknesses at the pore walls $t(\varphi)$ in front of and $t1(\varphi)$ behind the meniscus. (b) Functions of vapor pressure-dependent pore sizes $r(\varphi)$ according to Kelvin equation (1.37) and real size $r_R(\varphi)$ according to Eq. (1.79) considering sorption layer thickness.

with the constant M_γ from (1.68) for constant temperature T .

If for a real radius r_R one searches the associated but initially unknown relative humidity $\varphi(r_R)$, one can proceed iteratively using the following equation:

$$\varphi(r_R) = e^{\frac{M_\gamma}{(r_R - t(\varphi))}} \quad (1.80)$$

For a radius r_R of 1.0 nm, $\varphi(r) = 35\%$ and $\varphi(r_R) = 23\%$, for $r_R = 2.5$ nm follows $\varphi(r) = 66\%$ and $\varphi(r_R) = 59\%$ RH, compare **Figure 1.25b**.

1.4.6 Modeling of Adsorption Film Thicknesses

In the following, it is first investigated to what extent the basic isotherm for non-porous hydrophilic surfaces worked out in Section 1.4.2 can also be derived or approximated on the basis of thermodynamic approaches.

Furthermore, it is investigated to what extent the film thicknesses formed depend on the curvature of the surfaces and which film thicknesses can be formed in the pores within porous materials.

1.4.6.1 Modeling of Vapor Adsorption on Flat Nonporous Surfaces

The basis function equation $t(\varphi)$ (Eq. (1.50)) indicates to what extent a sorption layer or film of water molecules can be deposited **on flat surfaces of mineral solids**. The surface tension at the surface of the film, which may be several molecule layers thick, decreases from the surface tension of the solid γ_{SV} to the surface tension of water γ_L as a function of the distance from the surface and of the relative humidity above the film. **Figure 1.26** of Wu/Zandavi/Ward [44] shows this for water vapor and for heptane when acting on silicon surfaces.

By Adolphs/Setzer [30] and Churaev et al. [45] and others, the energy change occurring during film formation is described by the already quoted Eq. (1.61) and

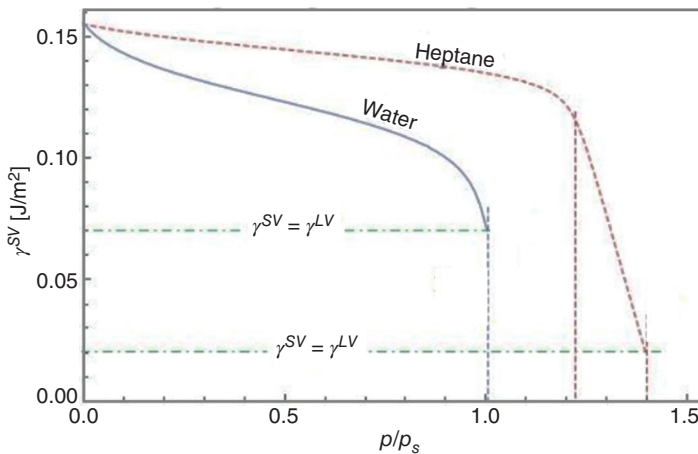


Figure 1.26 Course of surface tension or surface energy in sorption films upon exposure of a silicon surface to water vapor or heptane as a function of relative partial pressure. Source: Wu/Zandavi/Ward [44]/Royal Society of Chemistry.

the corresponding vapor pressure-dependent change in chemical potential (1.62), respectively, as follows:

$$\Delta\mu = RT \cdot \ln\left(\frac{p}{p_s}\right) \quad [\text{J/mol}] \quad (1.81)$$

At the same time, it must be possible to express the chemical potential in terms of the layer thickness itself, compare Adolphs/Setzer [30] and Churaev et al. [45]:

$$\Delta\mu = \Delta\mu_0 \cdot \exp\left(-\frac{n_{ads}}{n_{mono}}\right) = \Delta\mu_0 \cdot \exp\left(-\frac{h}{h_m}\right) \quad [\text{J/mol}] \quad (1.82)$$

Where n_{ads} = adsorbed liquid volume of the layer, n_{mono} = mono layer volume, h and $h_m = n_{ads}/\bar{V}_L$ and n_{mono}/\bar{V}_L , respectively, \bar{V}_L = molar volume of the liquid (water).

Since the change in chemical potential is also accompanied by a change in pressure (compare Eq. (1.36)), Eq. (1.82) can also be rewritten **as an equation for the “separating pressure” resp. “disjoining pressure”** to (see Churaev et al. [45]) for flat surfaces:

$$\pi(h) = \pi_0 \cdot \exp\left(-\frac{h}{h_m}\right) \quad [\text{Pa}] \quad (1.83)$$

The chemical potential in the sorption film must be in equilibrium with the vapor pressure according to Eq. (1.81):

$$\Delta\mu_0 \cdot \exp\left(-\frac{h}{h_m}\right) = RT \cdot \ln(\varphi) \quad \text{with } \varphi = \frac{p}{p_s} \quad (1.84)$$

The initially unknown $\Delta\mu_0$ must be determined via additional boundary conditions. We now pretend that $\Delta\mu_0$ is to be determined in such a way that the isotherm Eq. (1.84) for **the relative humidity** $\varphi_{mono} = 0.219$ takes the value n_{mono} , which corresponds to the sample sorption isotherm $t(\varphi)$. Resolving Eq. (1.84) to h **yields the layer resp. film thicknesses on flat surfaces as** $h = h_{plane}$:

$$h_{plane}(\varphi) = h_m \cdot \left(\ln\left(\frac{\Delta\mu_0}{RT}\right) - \ln(\ln(\varphi)) \right) = h_m \cdot \ln\left(\frac{\Delta\mu_0}{RT \cdot \ln(\varphi)}\right) \quad [\text{m}] \quad (1.85)$$

Equation (1.85) is first used to determine $\Delta\mu_0$. With h_m = mono layer thickness = 0.30 [nm] and $h_{plane}(\varphi_{mono})/h_m = 1$ it follows:

$$\Delta\mu_0 = RT \cdot \ln(\varphi_{mono}) \cdot \exp(1) = -1.006 \cdot 10^4 \quad \text{at } T = 293.15 \text{ [K]} \quad \text{with} \\ \exp(1) = e = 2.718.$$

Calculating now with this the resulting isotherm from Eq. (1.85), **we obtain the curve** $h_{plane}(\varphi)$ **shown in Figure 1.27 in comparison to the isotherm** $t(\varphi)$ from Eq. (1.50) according to [Franke]. There is surprisingly good agreement between the two curves.

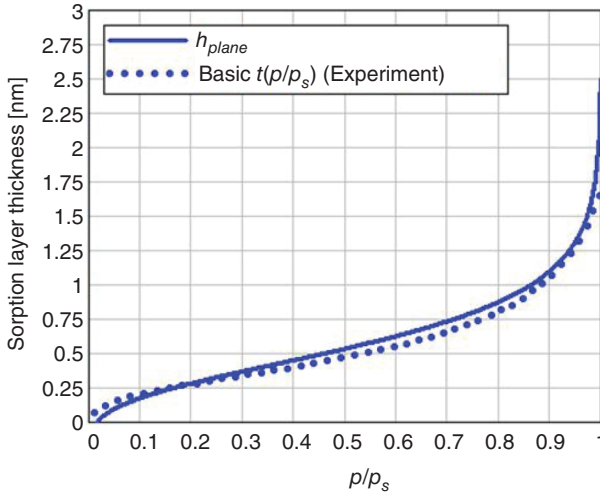


Figure 1.27 Comparison of sorption isotherms for plane surfaces of water vapor on mineral solids: h_{plane} according to Eq. (1.85) as well as the experiment-based basic isotherm according to Eq. (1.50).

1.4.6.2 Modeling of Sorption Film Thicknesses in Cylindrical Pores with Influence of Surface Curvature on the Thicknesses of Adsorbed Films

On concave surfaces of the inner wall of cylindrical pores influences not only the vapor pressure on the adsorbed film thicknesses but also an additional pressure from the surface tension of the curved sorbed liquid film, shown in **Figure 1.28a**. At equilibrium, the additional pressure component is Δp in [Pa] (**Figure 1.28b**).

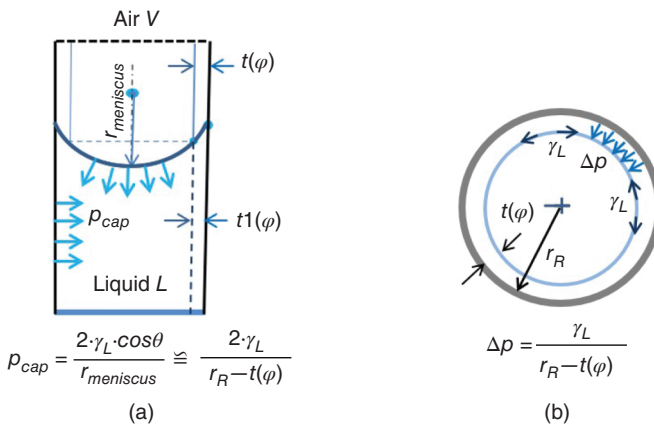


Figure 1.28 (a) Cylindrical capillary pore with meniscus and sorbed layer thicknesses at pore walls $t(\varphi)$ in front of and $t1(\varphi)$ behind the meniscus (b) functions of vapor pressure-dependent pore sizes $r(\varphi)$ according to Kelvin equation (1.37) and real size $r_R(\varphi)$ according to Eq. (1.79) considering sorption layer thickness.

The total pressure in the sorption layer can then be expressed as a change in chemical potential starting from the disjoining pressure for a concave curved surface.

$$\Delta\bar{G}_L = \bar{V}_L \cdot (\pi(h) - \Delta p) = -RT \cdot \ln\left(\frac{p}{p_S}\right) \quad (1.86)$$

In contrast to the explanations of Churaev et al. [45] or Mattia et al. [46], here Δp has a negative sign, since the pressure reduction in the liquid film must lead to a reduction in the chemical potential.

Using the relations (1.83) and (1.84), it follows after transformation

$$\frac{\Delta\mu_0}{RT} \cdot \exp\left(-\frac{h}{h_m}\right) = \frac{\gamma_L}{(r_R - h(\varphi))} \cdot \frac{\bar{V}_L}{RT} + \ln(\varphi) \quad (1.87)$$

After logarithmizing and transforming this equation, we obtain the relation for the resulting film thickness:

$$h(\varphi, r_R) = h_m \cdot \left[\ln\left(\frac{\Delta\mu_0}{RT}\right) - \ln\left(+\frac{\gamma_L \cdot \bar{V}_L}{(r_R - h) \cdot RT} + \ln(\varphi)\right) \right] \cdot 10^9 \quad [\text{nm}] \quad (1.88)$$

When calculating $h(\varphi, r_R)$, note that in the right part of the Eq. (1.87), h is also included. Therefore, in the 1st step, one calculates $h(\varphi, r_R)$ with an initial value $h = 0$ or $h = t(\varphi)$. One then repeats the calculation at least twice by inserting the result value $h(\varphi, r_R)$ of the equation into its right-hand part and then obtains a sufficiently high accuracy.

The disjoining-pressure part $\pi(h)$ in Eq. (1.86) is calculated in a number of publications using the **Hamaker constant A_H** . This constant describes the interaction between the involved molecules of solids and liquids and the influence of opposing material surfaces. The Hamaker constant A_H in the size of about 10^{-20} is in fact only approximately constant, compare literature Israelachvili [28]. The disjoining pressure fraction $\pi(h)$ in Eq. (1.86) formulated with the help of these constants can consist of up to three fractions depending on the physical influence taken into account with several physical parameters also known only approximately, compare calculations for example in literature Jing Li et al. [47] or the extensive explanations in Teletzke and Davis de L.E. Scriven [48].

This means that the calculated disjoining pressure values or resulting film thicknesses are also approximate values. Therefore, no further comments are made here with reference to the cited literature. However, the film thicknesses calculated in the manner described above obviously give a reliable indication of the existing dimension. Mattia et al. [46] also investigate the stability behavior of water films on the inside and outside of nano-capillaries made of quartz and carbon material. They use a Hamaker constant to model the disjoining pressure fraction and neglect the radius influence of the sorption layer thickness $h(\varphi)$ or $t(\varphi)$ on the growth of the films. Results on the behavior for convex cylinder surfaces are not reported.

On the convex outer surface of cylindrical material shapes, Eq. (1.86) also applies, but in this case, Δp must be given a positive sign, since now the surface tension generates a surface pressure. For the calculation of the corresponding

$h(\varphi, r_R)$, Eq. (1.87) also applies, whereby a minus sign must now be inserted before the term with γ_L . Proceed accordingly in Eq. (1.88). The calculation procedure then also corresponds to the procedure for concave surfaces.

The results of the film thickness calculations for concave and convex surfaces are shown in **Figures 1.29a,b and 1.31**. In **Figure 1.29a,b**, the film thickness profile is shown for cylindrical pores with constant radii of 2, 5, and 20 [nm] (and open ends) and corresponding external surfaces, respectively, as a function of relative humidity.

It can be seen that the film thickness at the inner surface of the pores increases faster with increasing relative humidity than for the reference curve plotted for flat

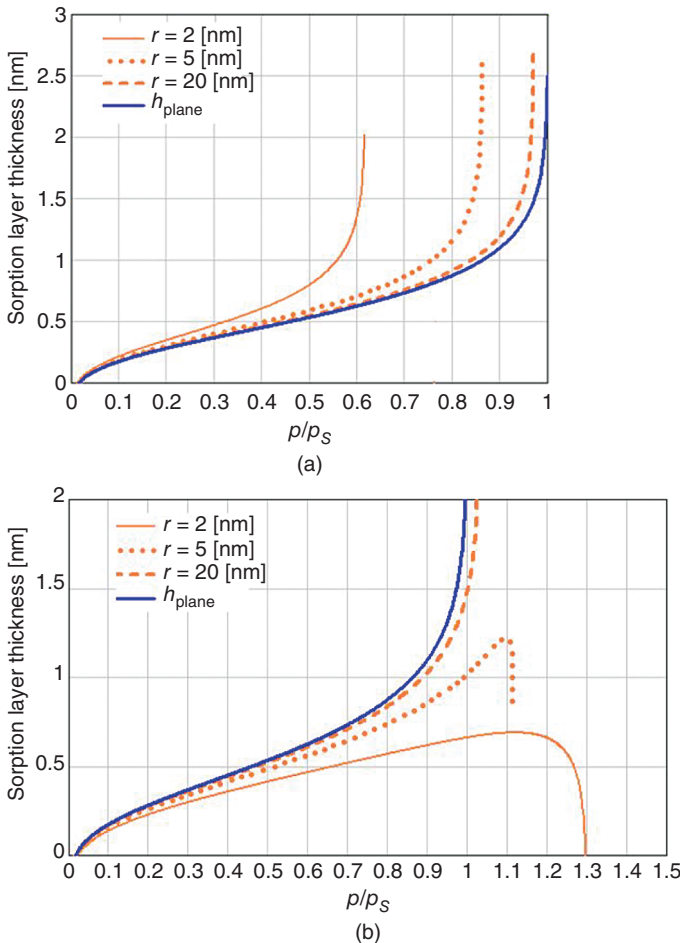


Figure 1.29 (a) Influence of surface curvature resp. radial tensile stress on adsorbed film thickness corresponding to **Figure 1.28b** in cylindrical pores at increasing RH compared to the film thickness function $h_{plane} \approx t(\varphi)$ for water vapor on flat surfaces (constant real pore radius $r_R = 2, 5, \text{ and } 20$ [nm]). (b) Influence of increased external vapor pressure on convex external surface of cylindrical material shapes compared to film thickness function $h_{plane} \approx t(\varphi)$ for water vapor on flat surfaces.

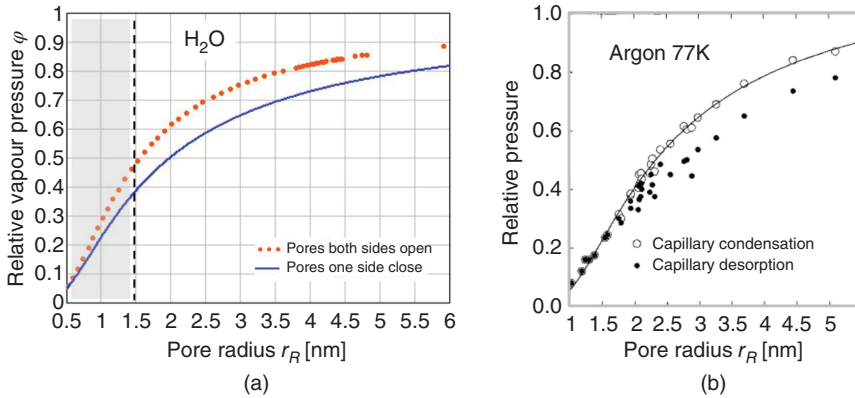


Figure 1.30 (a) Relative air humidities φ at which **filling of cylindrical pores** by condensed **water** occurs : **In pores open at both ends** up to radius of about 5 [nm] by collapse of inner surface film (calculated by Eq. ((1.88)), **in pores closed at one end** by classical capillary condensation from $r_R \approx 1.5$ [nm] for comparison. (b) **Experimental results** from [49] on the dependence of capillary condensation pressure and evaporation pressure on the pore radius in parallel cylindrical siliceous pores of MCM-41, for **argon** at 77 K.

surfaces for comparison $h_{plane} \approx t(\varphi)$. **Figure 1.29a** also shows clearly that, especially in the smaller pores, **film formation changes relatively spontaneously to pore filling in the sense of capillary condensation**.

As the calculation results according to Eq. (1.88) show, this occurs according to **Figure 1.30a** for cylindrical pores open on both sides up to a radius r_R of approx. 5 [nm] or an associated relative air humidity of up to approx. 85%. The comparison with cylindrical pores closed on one side, where a meniscus forms early starting from the closed end of the pore, using the extended Kelvin equation (1.80) in **Figure 1.30a** shows that capillary condensation starts earlier in such pores for a given pore radius r_R at lower vapor pressures or φ values as a function of the pore radius.

According to these results, for example, an initially empty longer cylindrical pore with a radius of 2 [nm] open at both ends fills completely with condensed water at about $\varphi = 62\%$, whereas the cylindrical pore closed at one end fills already at $\varphi \approx 50\%$. If we look at the desorption behavior of the pore open at both ends after filling, menisci now form at both ends, so that the onset of desorption corresponds to the blue curve in **Figure 1.30a**.

This results in a hysteretic adsorption–desorption behavior of such pores, which becomes more pronounced with increasing pore radius. The extent to which this mechanism is relevant to porous materials such as cement paste is discussed in Section 4.4.2.

If one considers the film thicknesses at the outer surface of cylindrical forms, the calculation yields the opposite result shown in **Figure 1.29b**. According to this, the film thicknesses are lower than for the reference curve $t(\varphi)$, especially at the smaller radii, as expected. There is no instability here up to relative vapor pressures of $\varphi = 1.0$. For this, vapor supersaturations $\varphi > 1.0$ are necessary, which can only exist under exceptional boundary conditions. For a surface radius of 2 [nm],

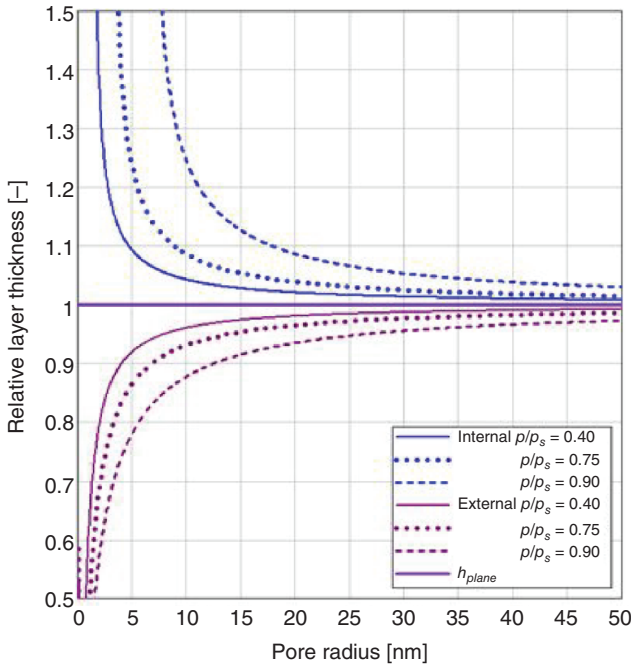


Figure 1.31 Comparison of relative film thicknesses on the inside of cylindrical pores and the outside of cylinders, taking into account capillary pressure (suction), as relative values related to the corresponding adhesion film thicknesses from water on a flat mineral surface (as a function of radius).

instability results at a φ value of 1.3, and for a radius of 5 [nm], instability results at φ about 1.1.

It was further investigated **the radius dependence of film thicknesses** in more detail for three selected relative vapor pressures, $p/p_s = 0.40, 0.75,$ and 0.90 . The calculation results are plotted relative to the layer thickness of the reference curve $t(\varphi)$ radius-dependent in **Figure 1.31**. One can see the strong tendency for increasing thickness differences at radii below about 10 [nm].

1.4.6.3 Volume of Adsorbed Water in the Not-yet-water-filled Pore Area

In the case of partial water saturation of the material, the Eq. (1.77) can be used to determine, for example, **the amount of water adsorbed in the not-yet-filled pore region** at different degrees of filling at the inner surface as a function of the relative air humidity φ .

For a given air humidity φ , Eq. (1.77) with lower limit $r_R(\varphi)$ and upper limit $r_R(\varphi) = r_R(0.9999)$ gives the adsorbed water volume stored in the unfilled pore region, denoted here by $\Delta Wh(\varphi)$.

The r_R -values of the integration limits for chosen φ are obtained from Eq. (1.79).

The dotted curve (color pink) in Figure 1.32 shows the calculated variation of sorbed moisture at increasing filling level or lower limit φ . At $\varphi = 1$, the sorbed volume is equal to 0, as expected, and exhibits the maximum at $\varphi \approx 20\%$ RH.

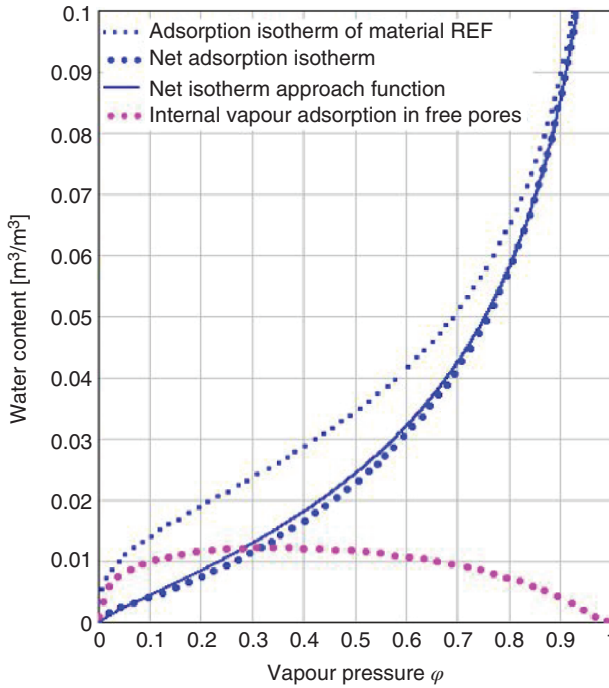


Figure 1.32 The adsorption isotherm of the material REF, the derived net storage function, and the curve of adsorbed vapor molecules from φ_1 to $\varphi_2 \approx 1.0$ (pink dotted) in the non-water-filled pore region.

The **net storage function**, which is important for all calculations of the internal surface area and moisture storage fractions, is calculated from the original storage function or adsorption isotherms by subtracting the fraction of the sorbed volume in the not yet filled pore region according to the following relation corresponding to **Figure 1.23a**:

$$\theta_N(\varphi) = \theta\varphi(\varphi) - \Delta Wh(\varphi) \quad (1.89)$$

In **Figure 1.32**, this yields the blue dotted curve as the net storage function for the material REF considered as an example, **calculated with the inner surface sorption**. The **dotted blue curve also included in the figure corresponds to the approximate curve used in Eq. (1.66)** in Section 1.4.4.1.

The curve $\theta_{r_N}(r_R)$ in **Figure 1.23b** is the net storage function Eq. (1.89) after conversion to r_R .

1.4.6.4 Film Thicknesses Due to Adsorption in the Water-filled Pore Region Behind the Meniscus, Estimation Using a Surface Energy Approach

In the large number of publications dealing with the question of film thicknesses on the inner surface of porous materials, the film thicknesses in the not yet water-filled pore region of the pores are always considered. The question of film thicknesses in the liquid-filled pore region behind a meniscus is not addressed, or

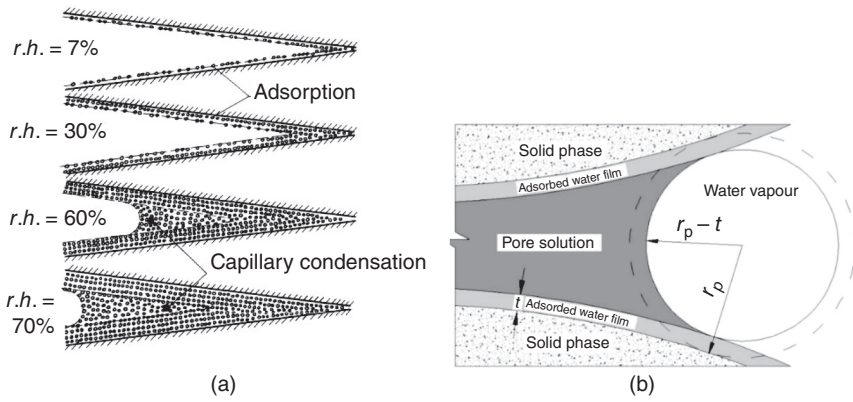


Figure 1.33 Schematic representation of capillary condensation in two different pore shapes with the assumption that the sorption film thickness behind the meniscus in the already water-filled pore region corresponds to the film thickness in front of the meniscus. (a) From Ahlgren [9]. (b) From Zhang et al. [50].

it is assumed that molecular layers sorbed there correspond to the total thickness in the nonliquid-filled pore region in front of the meniscus, compare the examples in **Figure 1.33a,b** from [9] and [50].

The international investigation results summarized in Section 1.4.7 largely agree in the statement that due to sorption of water molecules and ions in aqueous solutions film thicknesses of high toughness at least about 2 monolayers thick are formed. A consideration of this situation in the water-filled pore region behind the meniscus is therefore necessary, since according to these results, a probable **non-negligible influence in the modeling of moisture transport** arises.

To estimate the film thicknesses addressed, a theoretical consideration on film thickness evolution is given below, which starts from the following Gibbs–Duhem equation (1.90), derived from the well-known Gibbs energy equation with surface energy influence and describing the enthalpy at equilibrium for constant temperature and constant external pressure.

$$\sum n_i \cdot dn_i + A \cdot d\gamma = 0 \quad A = \text{surface} \quad (1.90)$$

This equation makes clear the direct relationship between chemical potential and surface energy, which will be used below.

Dash and Peierls [51] gives the related equation $d\gamma = -n \cdot d\mu$ with μ as chemical potential and n as sorption layer thickness to characterize sorption film thicknesses. However, concrete layer thicknesses are not derived from Dash.

It is assumed that the chemical potential starting from the solid surface decreases as follows according to the well-known approach, for example, Churaev/Setzer [52] or the course of the disjoining pressure approach Eq. (1.83):

$$\Delta\mu(h) = \Delta\mu_0 \cdot \exp\left(-\frac{h}{h_m}\right) \quad (1.91)$$

For this, it is necessary that the solid surface has a larger surface energy than the liquid or water, according to the condition for spreading given by Eq. (1.10). As shown

by Wu/Zandavi/Ward [44], **compared to Figure 1.26**, it is assumed that the surface energy within the surface film must change from γ_{SV} to γ_{LV} .

The number of moles per m^2 area per monolayer is

$$z_m = \frac{h_m \cdot A}{\overline{V}_L}$$

With the surface energy γ_{SV} [$Nm/m^2 = J/m^2$] of the solid surface A , the associated change in the chemical potential of the 1st molecular layer related to the molar volume \overline{V}_L is now formulated as follows:

$$\Delta\mu_0 = \frac{\gamma_{SV} \cdot A}{z_m} = -\frac{\gamma_{SV} \cdot \overline{V}_L}{h_m} \quad (1.92)$$

In the present approach, the chemical potential changes from the film thickness h_{max} to the value of bulk water γ_L , i.e. the chemical potential is reduced by the value $\Delta\mu_{h_{max}}$:

$$\Delta\mu_{h_{max}} = -\frac{\gamma_L \cdot \overline{V}_L}{h_{max}} \quad (1.93)$$

Substituting the Eqs. (1.92) and (1.93) into (1.91), we obtain the equation **for the total film thickness h_{max} sought for a plane solid surface covered with bulk water**:

$$\exp\left(-\frac{h_{max}}{h_m}\right) = \frac{\gamma_L}{\gamma_{SV}} \cdot \frac{h_m}{h_{max}} \quad (1.94)$$

The results resulting from Eq. (1.94) are explained in the following:

First, the **influence of the capillary pressure from the meniscus, which is to separate the liquid filling in the considered pore region from the not yet filled pore region**, shall still be considered.

Let the capillary suction on the inner pore surface, which depends on the vapor partial pressure at the concave surface of the meniscus, be denoted by $\Delta p_{cap}(\phi)$ with $\phi = p/p_S$.

It is assumed that this results in a change of the chemical potential of the liquid and also in the influence of thickness h_{max} accordingly:

$$\Delta\mu_{1h_{max}} = -\left(\frac{\gamma_L}{h_m} + \Delta p_{cap}(\phi)\right) \cdot \overline{V}_L \quad (1.95)$$

In it, with Eq. (1.34) and considering the Kelvin equation

$$\Delta p_{cap}(\phi) = \frac{2 \cdot \gamma_L}{r_{meniscus}(\phi)} = -\frac{RT \cdot \ln(\phi)}{\overline{V}_L} \quad (1.96)$$

Substituting Eq. (1.96) into Eq. (1.95) and then combining it with Eqs. (1.91) and (1.92) gives the equation for **the film thickness h_{max} for the inner surface of water-filled cylindrical pores under capillary suction influence** at given vapor

partial pressure $p/p_s = \phi$:

$$\exp\left(-\frac{h_{max}}{h_m}\right) = \frac{\left(\frac{\gamma_L}{h_{max}} + \Delta p_{cap}(\phi)\right)}{\frac{\gamma_{SV}}{h_m}} \quad (1.97)$$

From the Eq. (1.97), the film thickness can now be estimated as a function of the capillary pressure in filled pores or the relative vapor pressure ϕ . To solve the equation, $h_{max} = h_m \cdot x$ is set. The results can be obtained from **Figure 1.34**.

The value $x = 2.5$ molecule layers would be assigned to narrow pores, 4.4 molecule layers or approx. 1.3 [nm] to planar, water-covered silicate surfaces.

The following values were used for calculation: $\gamma_{SV} = 1.4$ [J/m²] for silicate hydrates and HCP, respectively, $\gamma_L = 0.073$ [J/m²], $h_m = 0.30$ [nm] or $0.30 \cdot 10^{-9}$ [m] as monolayer thickness for water, \bar{V}_L = molar volume of the liquid (water).

The measured value given by Zhao et al. in literature [53] for film thicknesses in bulk-water on muscovite mica is 0.9 [nm], compare **Figure 1.39b**. The **film thicknesses for water-filled pores** estimated here by calculation as a function of capillary pressure are 2.5–4.4 molecular layers and 0.75–1.3 [nm] for water on silicates, respectively. From these results, it can be concluded that a simple “extension” of **the film thicknesses determined in the non-water-filled pore region in front of a meniscus into the water-filled region is not readily possible and justified**. Therefore, the behavior of the film thickness trajectories assumed in **Figure 1.33a,b** cannot be adopted in this way, which is supported by the investigation results in Section 1.4.6.5.

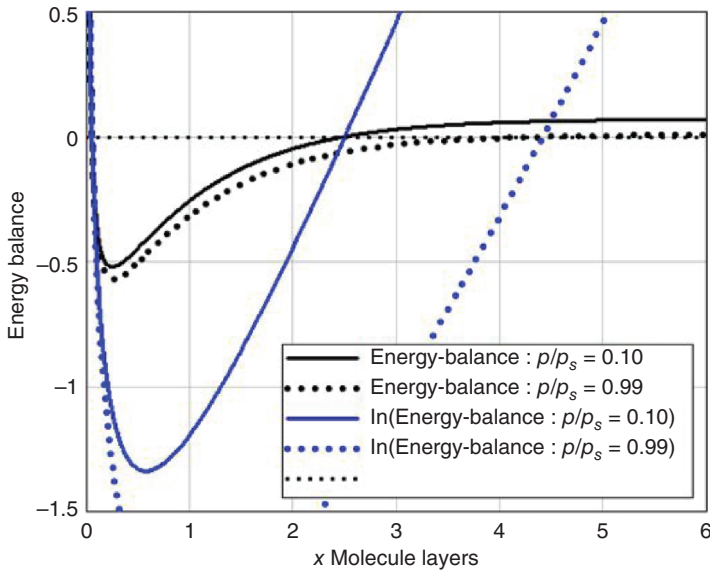


Figure 1.34 Calculated film thicknesses on the inside of water-filled cylindrical pores via a surface energy approach. The intersections of the curves with the zero line give the number x of molecular layers of the sought film thicknesses $h_{max} = h_m \cdot x$. For $\phi = 0.99$ RH: $x = 4.4$ layers and for $\phi = 0.10$ RH: $x = 2.5$ layers.

1.4.6.5 Volume of Adsorbed Water Molecules on the Inner Surface in the Water-filled Pore Area

In Section 1.4.7, results of experimental investigations and molecular-dynamic (MD) studies are reproduced on the question of adsorbed water-molecule films at the inner surface in the water-filled pore region.

Reported are, among others, the results of capillary water transport experiments on nanopores, according to which stable surface films of 0.4–0.6 [nm] thickness (Xu et al. [54]) or 0.60 [nm] thickness (Gruener et al. [55]) are formed on the inner surfaces of the pores. These adsorbed films constrict the pore cross sections and do not themselves participate in fluid transport.

K. Wu et al. [56] evaluates 50 corresponding studies and finds a nonparticipating film thickness of about 0.7 [nm] and a “dramatic” increase in viscosity of the adsorbed films at pore diameters ≤ 1.4 [nm].

Antognozzi et al. [57], Zhao et al. [53], and Arai et al. [58] determine using AFM that tough molecular layers of at least 0.70 [nm] form on surfaces with behavior different from bulk water.

The theoretical consideration undertaken in Section 1.4.6.4 based on the surface energy of adsorbed films yields a sorption thickness between 2.5 and 4.4 molecular layers, on average order of magnitude 0.90 [nm].

Knowing the sorption film thicknesses in the water-filled pore regions is of high importance for understanding and modeling moisture transport in porous materials. Therefore, for the sample material REF, it was computationally determined which water content fraction results in partial or complete water saturation of the material, if constant adsorption film thicknesses are taken as a basis in the order of magnitude of the previously mentioned, experimentally and theoretically determined values.

Film thicknesses $t_{film} = 0.30, 0.45, \text{ and } 0.60 \cdot 10^{-9} = \text{const. [m]}$ were used in the calculation.

The following relation was used for this purpose:

$$\Delta V_{film}(\varphi_1) = \theta_N(\varphi_0) + t_{film} \cdot \Delta A(\varphi_0, \varphi_1) \quad (1.98)$$

Then, to an initial value $\theta_N(\varphi_0)$ is added the water volume, which is the product of the film thickness t_{film} and the inner surface area $\Delta A(\varphi_0, \varphi_1)$ between the initial φ_0 and the running upper φ_1 boundaries. $\theta_N(\varphi_0)$ is the water content of the net adsorption curve at a pore radius of a water molecule $r_R(\varphi_0) = 0.30 \cdot 10^{-9}$ with $\varphi_0 = 0.0116$. $\Delta A(\varphi_0, \varphi_1)$ corresponds to the area integral (1.77).

For smaller φ values, the volume from film thickness and surface area partially exceeds the existing pore volume. It is then set equal to the corresponding volume of the net storage function.

The result of the calculations can be seen in Figure 1.35. It can be seen that for a film thickness of 0.30 [nm], the pores are filled with adsorbed water up to $\varphi \approx 20\%$, for a film thickness of 0.45 [nm] up to $\varphi \approx 40\%$, and for a film thickness of 0.60 [nm] at relative air humidity up to $\varphi \approx 55\%$. These conditions have an appreciable effect on moisture storage and transport in a pore system, which must be taken into account when modeling moisture transport.

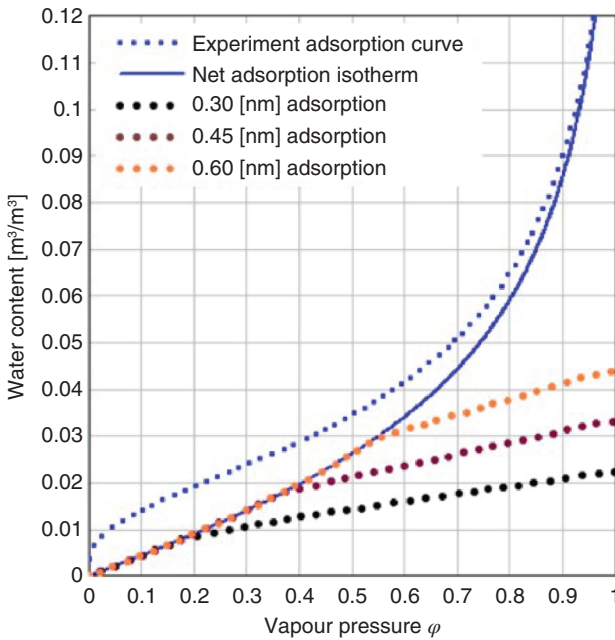


Figure 1.35 Adsorption isotherm of the material REF and net storage function and volume of adsorbed water molecules at the inner surface in the water-filled pore region with film thicknesses of 0.30, 0.45, and 0.60 [nm]. The net adsorption isotherm shows the water content of the pore system up to the considered value φ , without the moisture content adsorbed on the inner surface in the non-filled pore area above.

1.4.7 Molecular Simulations and Experimental Investigations on the Dimension of Adsorbed Film Thicknesses (International Research Results)

With the help of computer programs, that simulate via modeling, the interactions between molecules and atoms to their motions, mergers and attachments, it is possible to estimate the sorption of liquids on solids or resulting film thicknesses. For years, programs have been used for this purpose, known as **MD or MDS** as molecular dynamics simulations, which are further developed for simultaneous description of chemical reactions under the name molecular mechanics, in the last stage as **reactive molecular dynamics (RMD)**, which obviously require very large computational effort, for example, require the use of parallel computers, compare H.M. Aktulga et al. [59]. An overview of the state of development and available programs is given by K. Farah et al. [60].

Castrillon et al. [61] reports in his paper the results of **MD simulations** on sorption of water films on quartz surfaces. Among other things, the distribution of density and local potential energy near the surface is also reported. Castrillon, extending his calculations to water molecule thicknesses corresponding to about 15 monolayers, finds an influence on the water-molecule orientation up to a distance

of about 1.4 [nm] from the surface and **a firmer bond or stiffness (H-bonding) of the water-molecule layers up to a thickness of 0.4–0.6 [nm]**.

However, the results of calculations with current computer programs always require confirmation by the results of experimental investigations:

The development of AFM or surface force apparatus (SFA) technique now allows additional insight into the formation of film thicknesses at interfaces. The paper by Israelachvili et al. [62] provides an overview of the status of this development up to 2010. In these devices, an upper tip (guided by special piezoelectric crystals) is gradually moved in small air-conditioned chambers to the material surface to be tested, which may be covered with a liquid film thickness. The exact distances are measured using light wavelengths or laser technology.

Figure 1.36 shows schematically the structure of an AFM. The caption provides more information about the function. A recent overview of the state of AFM technique can be found from Peng et al. [63]. Problems concerning the interpretation of the results of conventional AFM technique with tip insertion are discussed in [64]. An overview of other investigation techniques used, such as NMR and X-ray techniques, can be found in Monroe et al. [65].

In the work of Xu et al. [54], permeability experiments and subsequent MD simulations are reported. In particular, transport experiments are performed on fine porous material of Vycor glass with mean pore diameters of 3.4 and 7.2 [nm] and on porous quartz material Xerogel with mean pore diameters of 3.4 [nm]. Aqueous solutions with 1M NaCl and 1M CaCl₂ are also used for comparison.

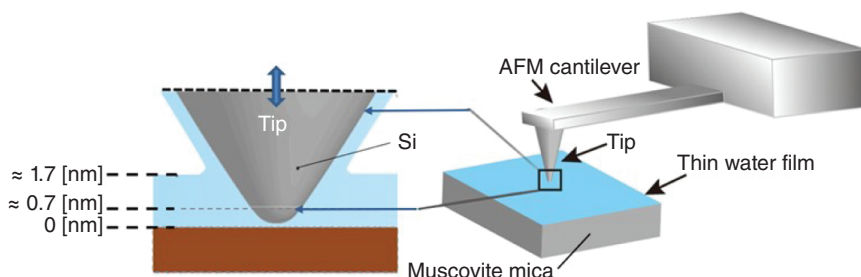


Figure 1.36 Schematic representation of the principle of an AFM (atomic force microscope) inside a temperature and humidity adjustable measuring chamber. A very fine tip attached to a cantilever is moved over the area of the interface to be measured, horizontally in 2D or/and vertically in 3D scanning. The tip or curved surface can be guided into the liquid film in Ångström steps. The path of the tip is measured by a laser apparatus or a light wave interference system, and the ultra-small forces occurring at the tip are measured via the spring stiffness of the cantilever. The cantilever can also operate above the interface with the solid submerged in the liquid. The cantilever can be operated in static mode or in dynamic mode (near its resonance frequency), in the latter case frequency-modulated as FM-AFM or amplitude-modulated as AM-AFM. Source: The pictorial elements shown here are taken from Arai et al. [58]/Springer Nature/CC BY 4.0. The measurements of Arai et al. were made in saturated water vapor atmosphere on interface to muscovite mica. The nanometer dimensions given in the figure are measurement results: up to about 0.7 [nm] a tough molecular layer was measured, covered up to about 1.7 [nm], with bulk water.

In both the experiments and the MD simulations, respectively, it is found that the material pores have a 2-layer water-molecule film of about 0.6 [nm], which leads to a corresponding narrowing of the pores during moisture transport. There were no significant changes when sodium chloride and calcium chloride solutions were used.

S. Gruener et al. [55] perform capillary water uptake experiments on Vycor glass with mean pore diameters of 3.4 and 4.9 [nm]. The analyses revealed surface films not participating in moisture transport on the order of 2 molecule layers.

Asay and Kim [66] performs infrared spectroscopic ATR (attenuated total reflection) studies on flat silicate surfaces at 20 °C and increases the relative humidity of air and finds that an approximately 3 monolayer thick water film of an “icelike” nature forms on the silicate surface.

K. Wu et al. [56] evaluates the results of more than 50 different studies on the question of the formation of water-film thickness using a model based on Hagen-Poiseuille’s theory to describe water transport in cylindrical pores in the presence of film thicknesses on the inner pore walls. The theory is applicable to pore diameters >1.4 [nm], since a dramatic increase in viscosity occurs for smaller diameters. Wu’s comparative calculations lead to the conclusion that, especially for pore diameters <10 [nm], there is an increase in viscosity for hydrophilic materials compared to bulk water, while a large decrease in transport resistance occurs for transport processes in hydrophobic materials. In hydrophilic materials, according to Wu, an approximately 0.7 [nm]-thick stable film thickness is formed on the inner surfaces.

Antognozzi et al. show in [57] results of measurements on thickness-dependent shear viscosity on a glass/mica combination, determined with a transverse dynamic force microscope (TDFM). A section of an optical glass fiber with plane-cut surfaces is used as a tip and guided in dynamic shear motions over water films of different thicknesses on a muscovite mica surface. The experiments show, that below about 0.9 [nm], there is a dramatic increase in shear viscosity or shear stiffness of the water-molecule layers between the glass surface and the mica.

This increase in stiffness therefore occurs below a film thickness of 0.45 [nm] with respect to one of the two material surfaces.

Figure 1.37 shows AFM results and MD calculations from Kimura et al. [67]. These analyses were performed at the interface between muscovite mica and an upstanding 1M KCl aqueous solution. According to the results of Martin-Jimenez et al. [68], ion concentrations ≤ 1 M have only a minor influence on the structure of the water-molecule layers, compare the following remarks. From the results shown in **Figure 1.37**, it can be concluded that a film thickness of 0.45 [nm] was also present, according to the results of Antognozzi et al. From these results, it can be concluded that, at least for low-concentrated electrolyte solutions (or pure water), a primary sorption layer thickness of about 0.45 [nm], already determined by Kimura et al. and Antognozzi et al., can be assumed. Furthermore, it follows from the present work that primary layers of greater thickness result at higher electrolyte concentrations.

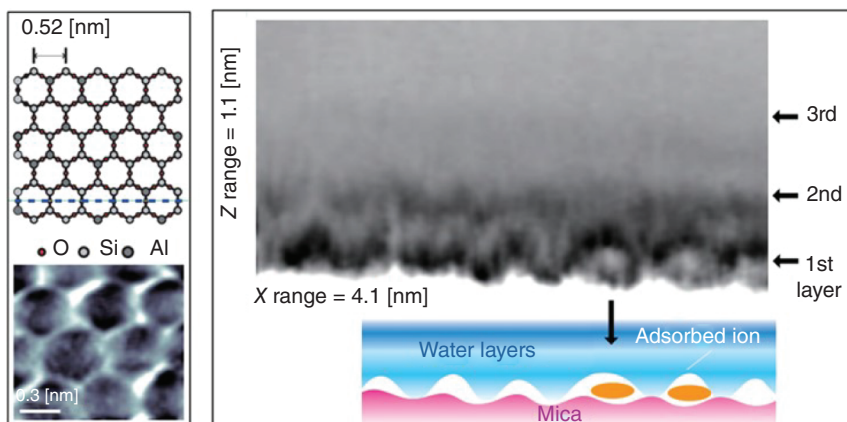


Figure 1.37 Results of 2D force scanning of the muscovite mica material interface perpendicularly into the overlying 1M KCl aqueous solution using FM-AFM. **The left part** schematically shows the crystalline structure of the mica. Below is the microscopic AFM image of the corresponding surface when scanning the surface. This cleaved mica surface corresponds to a structural section corresponding to the blue-dashed line in the schematic structure image above. **The right part** shows the registered structure in the aqueous solution above the mica surface. At the muscovite mica/water interface, the water molecule layer penetrates into the center of the hexagonal structure schematically illustrated on the left. In the upper layers, fluid water molecule layers are observed, and they show a smaller correlation with the surface structure. The layers registered by the authors are indicated at the right edge of the image. The total image height is 1.1 [nm]. The yellow particles in the sub-image are likely to be K^+ ions or hydrated K^+ ion complexes adsorbed on the surface. Source: Kimura et al. [67]/AIP Publishing.

By Martin-Jimenez et al. [68] present further insightful investigation results on 3D structure at interfaces. Figure 1.38 contains some results of these investigations and related details. Further results of this work can be reproduced as follows:

The interaction with the mica is found to have a nearly complete monolayer of cations at low salt concentrations (0.2M), as indicated by the AFM images. The K^+ ions from the solution occupy the positions in the cleaved plane previously occupied by K^+ ions in the bulk mica crystal. The water molecules from the first hydration layer are tightly bound to the solid surface, occupying the space between the cations. The second hydration layer is placed 0.25 [nm] above the adsorbed K^+ ions and it follows its atomic corrugation. The water molecules in the 2nd layer are centered on top of the cations of the first layer, but with a larger lateral spreading. The accompanying DFC simulation predictions show a significant reduction of the cation coverage of the mica at low salt concentration.

At higher salt concentrations (3–5M), the interfacial layer has a different structure and composition. It is thicker and shows a crystal-like structure.

The observed phenomenology is not restricted to KCl solutions. It also applies to other alkali halide electrolyte solutions.

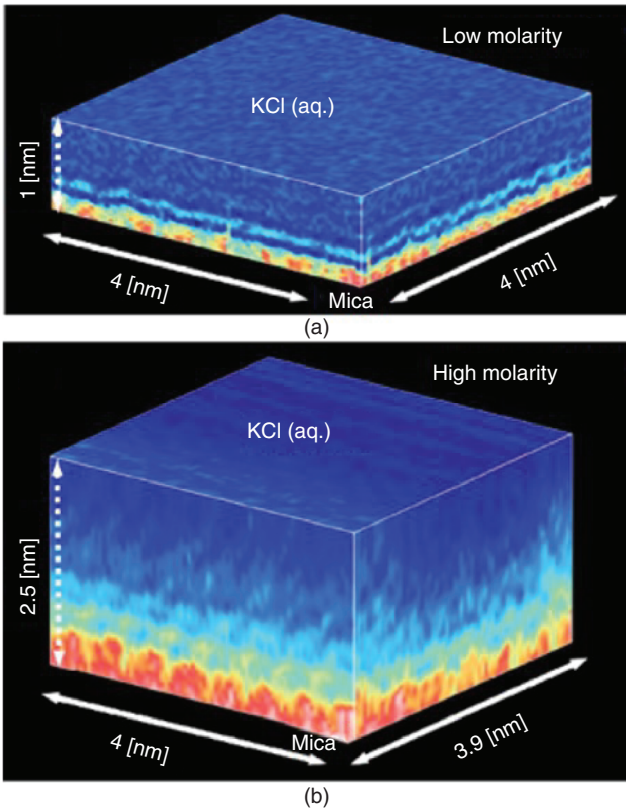


Figure 1.38 Three-dimensional AFM-images of muscovite mica/electrolyte solution Interfaces. (a) 3D AFM image of a KCl (aq.) solution (0.2M KCl). The image shows a monolayer resp. interface of partial adsorbed K^+ ions (light red) topped by two hydration layers (lighter stripes), following the atomic corrugation of the mica surface. (b) 3D AFM image of a mica-KCl (aq.) interface (4M KCl). The interface is divided into two main regions: an ordered liquid layer extending up to 2 [nm] from the mica surface into the bulk solution above it. These 3D maps show the variations of the phase shift of the tip's oscillation. The 3D AFM experiments were performed at 300 K. Source: Martin-Jimenez et al. [68]/Springer Nature.

The results reported by G. Zhao et al. in [53] are particularly remarkable as well. Figure 1.39a,b shows selected results of the investigations with a SFA 2000 apparatus.

These AFM investigations have the special feature that the conventional tip configuration was not used, but instead 2 cylindrical surfaces (tube sections with a radius of 2 [cm]) were arranged in a crossed configuration opposite each other. Both crossed cylindrical surfaces were covered with a cleaved layer of muscovite mica. The mutual distance of both surfaces was measured in the AFM in steps of 0.1 [nm] using the MBI lightwave interference technique FECO, using a video camera to allow direct monitoring of the surface separation and phase change of the adsorbed water between two mica surfaces. More Details of the measurements

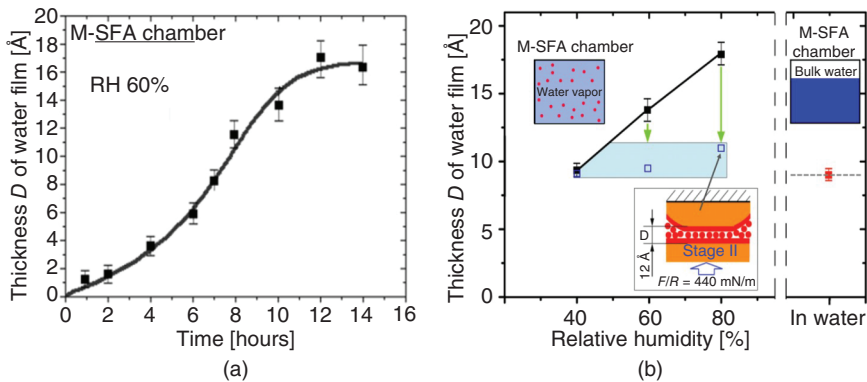


Figure 1.39 Measurement results of G. Zhao et al. from [53] on water vapor sorption on muscovite mica (measured with SFA 2000 measuring apparatus). (a) Time-dependent evolution of sorption film thickness from water on muscovite mica under constant vapor pressure. (b): The black squares give the measured values of the formed film thicknesses as a function of vapor pressure at sufficient distance of the opposing surfaces. When the surfaces are automatically moved together, part of the original water film is reduced. This process comes to a halt due to corresponding counterforce at a mutual distance of the muscovite surfaces in the order of $D = 0.90$ [nm] after 10 hours, which leads to a layer thickness of $D/2 = 0.45$ [nm] related to each of the two surfaces, if the feed force is not significantly increased. The solid square symbols indicate the initial thickness of the measured adsorbed water film at the moment of two mica surfaces contacting together. The hollow square symbols indicate the film thickness reduced to the light blue area under the action of the external load schematically shown by the sub-picture below. **In the right part of the figure (b)** the corresponding measured value of approx. 0.9 [nm] after approx. 10 hours pressure at 80% RH results, when the experiment is carried out **in water**. This result also corresponds to an individual layer thickness of 0.45 [nm] per surface. Source: Zhao et al. [53]/AIP Publishing.

can be taken from **Figure 1.39b** or the corresponding figure caption. Some relevant details will be presented here in addition:

After vapor adsorption process, over hours at sufficient distance between the mica surfaces, the opposing mica surfaces are pressed together with the pressure value mentioned in the sub-figure of **Figure 1.39b**. A film of water molecules of thickness of about 0.45 [nm] is formed under this pressure. The authors describe the state of this film as similar to solid that cannot flow easily.

In following experiments, the stability of this film under sustained compression was tested. It is found that creeping occurs at which after hours, the layer thickness was reduced approximately to half. They conclude that the primary layer (of 0.45 [nm]) of the adsorbed water is unstable under the action of an external load and its property is similar to an ice-crystal structure that will creep under the action of an external load even with a smaller pressure.

Separation tests after compression were also performed. In this case, the separation between two rigid solid surfaces happens without any capillary condensation. It is found that the adhesion force increases with the relaxation time when the mica surfaces are bridged by the first layer of the adsorbed water film.

Figure 1.39a shows the results of time-dependent adsorption experiments: after 10 hours at 60% RH/25 °C an adsorption layer thickness of $D/2 \approx 0.70$ [nm] was formed on the mica surface due to the vapor pressure in the test chamber. These results on 12 independent measurements, each with new muscovite surfaces, show a time dependence of the sorption process. Information on the related air/vapor velocity in the measuring chamber was not provided.

In Section 1.4.6.4, the question was asked at the beginning: Can one really assume that the sorption film thicknesses at the pore walls to be expected in the water-filled pore region correspond to the vapor pressure-dependent adsorption film thicknesses that are present in the open pore fraction not yet filled with water?

From the present book section and the preceding Sections 1.4.6.4 and 1.4.6.5, **it is now clear that there is no correlation between the sorptive film thicknesses in these two regions.** Films from vapor sorption with thicknesses of up to about 1.7 [nm] can be expected at high RH, while in the water-filled region films formed on the pore walls have a structure deviating from bulk water up to thicknesses of at most about 0.70 [nm], and which exhibit ice-crystalline properties at thicknesses \leq about 0.45 [nm]. According to previous findings, this is true for hydrophilic interfaces to pure water or aqueous electrolyte solutions with concentrations \leq approx. 1M.

For higher concentrated aqueous electrolyte solutions, significantly higher film thicknesses must be assumed, compare [68].

The analyses of ion concentrations in the pore solution of HCP from Portland cements according to EN-197 yield concentrations of at most $\approx 0.30M$, compare Lothenbach et al. [69] and Kenny/Katz [70]. The vast majority of ions in the hydrated state of the cements consist of potassium and sodium ions. The ion concentration in hydrated hardened cement paste decreases drastically when increasing amounts of fly ash are used [70].

From the experimental studies, especially by G. Zhao et al. [53], it appears that mutual compression from opposing surfaces makes the adsorption films thinner, but they apparently adopt an even more stable consistency.

Therefore, the question is to be asked whether, for example, the **decrease in permeability during a pressure test** with high pressures when determining the hydraulic conductivity can also be attributed to a parallel solidification of formed adsorption films, compare Section 3.1.8.1.

1.4.8 Influence of Adsorption Films on Meniscus Formation and on Capillary Pressure in Capillary Pores

In Section 1.3, the basic relationships of fluid uptake in porous materials as a result of surface energetic conditions were discussed. A distinction was made between fluid uptake due to capillary suction and fluid storage due to condensation from the penetrating vapor phase. The investigations in the previous sections showed that **different adsorption layer thicknesses can form behind a meniscus in the water-filled pore region and in front of the meniscus**, which meet each other in the region of the meniscus.

At $\varphi = 50\%$, according to Section 1.4.6.5, an adsorption film thickness of about 0.7 [nm] is present behind the meniscus, while in front of the meniscus, the adsorption film thickness from the vapor phase is about 0.50 [nm] (**Figure 1.28a**). This raises the question of the **consequences for the formation of the meniscus and its edge angle to the pore surface**, and thus for an influence on the capillary pressure. Related to this is the question of fluid storage potential by suction or capillary condensation.

Numerous publications have investigated **what shape the fluid surface of a meniscus takes at the transition to the pore wall**. Cited here are only the papers by Churaev et al. [52] and Kuchin and Starov [72], from which **Figure 1.40a,b** were taken.

In **Figure 1.40a**, the shape of the menisci at complete wetting (2) and partial wetting (1) with associated edge angle is given in the figure scale. Furthermore, an adsorption film h_e at the pore inner surface of thickness 1.85 [nm] is assumed there. This is a film thickness present at the basic isotherms for flat surfaces used here at a relative vapor pressure of $\varphi \approx 99\%$ (compare **Figure 1.27**). The corresponding calculated shapes of the liquid surface at the transition of the meniscus to the pore wall are given in detail for the partial wetting case in **Figure 1.40b**.

Particularly in the presence of larger film thicknesses of, for example, $t = 1.5$ [nm] (in front of the meniscus), the question remains, despite the theoretical modeling results of Kuchin (**Figure 1.40b**), for example, to what extent a force transfer from a meniscus to the pore wall in the longitudinal direction of the pores into the membrane surface of the film may be assumed.

This mainly concerns situations where liquids are transported by capillary suction in a pore system whose pore walls are covered by said liquid film. It must be taken into account that the liquid molecules below the film surface are largely in the bulk state in the case of thicker films. Notable forces in the form of shear stresses cannot

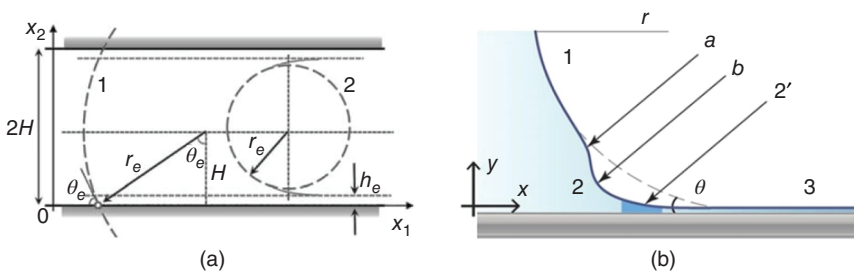


Figure 1.40 Figures and results of modeling from Kuchin et al. [71] and Kuchin and Starov [72]. (a) Representation of the shape of the menisci in total wetting (2) and in partial wetting with the corresponding contact angle θ_e . (1) (b) Liquid profile in a capillary in the case of partial wetting in the state of local equilibrium at excess pressure $P \neq P_e$; r and θ are the radius of the spherical meniscus in the central part of the capillary and the new local equilibrium contact angle ($\theta \neq \theta_e$) (1) Spherical meniscus of a new radius r , where $r \neq r_e$; (2) profile of part of the transition zone at local equilibrium with the meniscus; (3) flat equilibrium liquid film of thickness h_e , with old equilibrium excess pressure P_e ; (2') a flow zone inside the transition region. Source: Kuchin et al. [71] and Kuchin and Starov [72]/American Chemical Society.

be transmitted to the pore wall in this region, if the results of research work are interpreted accordingly.

According to the results, for example of [73], [74], and [75], when shear stresses are applied, **slipping takes place between the film surface and the firmer approximately 2 molecule-layer-thick layer** on the material surface. Only when approaching the pore wall does the surface free energy in the adsorbed film increase according to the Sections 1.4.7, 1.4.6.1, or 1.4.6.4, and thus the ability to absorb the edge stress from the meniscus.

This is also clear in the approaches to disjoining pressure in adsorption films by, for example, Churaev et al. [52] and Kuchin et al. [71]. Also, Schimmele et al. [76] assumes that, especially at contact angles $\geq 0^\circ$, the meniscus edge force is introduced into the “load-bearing” pore wall.

From this, the assumption could be derived that the force transfer from a meniscus in the mentioned transport situation (with the occurring molecular slipping) is always transferred into the “solidly” adsorbed surface layer about 2 molecule layers thick, according to **Figure 1.41a,b**.

Systematic investigations of this question on capillaries with different inner film thicknesses, generated from different relative humidities of air, have probably not been realized so far because of experimental difficulties.

Behavior as assumed in **Figure 1.41a,b**, on the other hand, could be **unjustified in the case of capillary condensation in pore systems**, where increasing pore filling occurs not by suction but by condensation from the vapor phase. In this case, a stress equilibrium between meniscus edge force and pore-film surface is conceivable in the region of the meniscus transition, depending on local conditions, without any appreciable effect of a slipping influence.

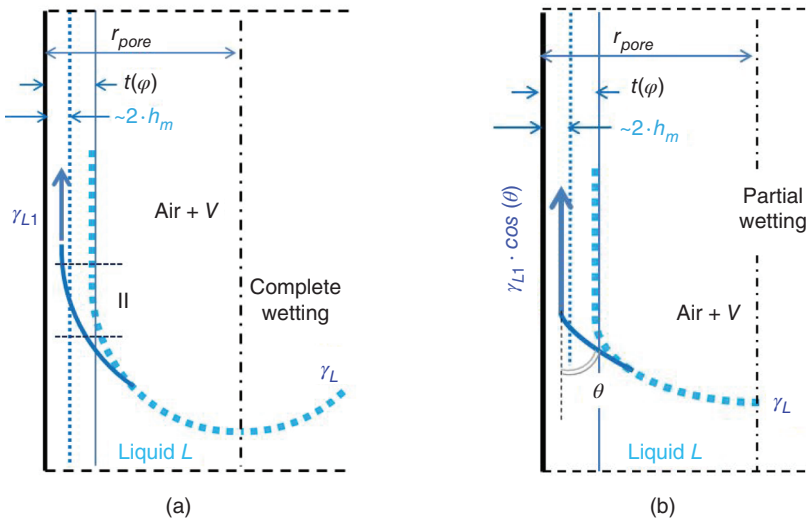
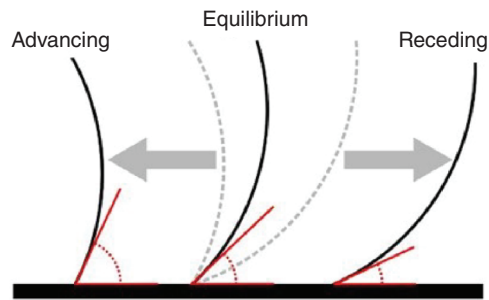


Figure 1.41 Modeling of the force transmission from the meniscus edge into the area of the contact zone. (a) Complete wetting with contact angle $\theta \approx 0^\circ$. (b) Partial wetting with contact angle $\theta \geq 0^\circ$.

Figure 1.42 Schematic illustrated behavior of the shape of the menisci and the contact angles in a pore system during fluid adsorption (advancing meniscus) or fluid desorption (receding meniscus). Source: Andrew et al. [78]/with permission of Elsevier.



However, compared to equilibrium, a flattening of the meniscus takes place in the case of water absorption by vapor sorption and an increase of the curvature in the case of drying processes. Many publications attempt to model this process, see Starov and Velarde [77] and Kuchin and Starov [72]. Measured values on the phenomenon are reproduced, for example, in [78] and [79].

With capillary fluid uptake, a flatter meniscus and larger edge angle usually establishes itself because of the lower initial transport resistance, which transitions to the equilibrium position when transport stops. The degree of change of the edge angle depends on the particular transport resistance, see Popescu et al. [80] and **Figure 1.42**, for instance. Many publications are concerned with this question resp. **the shape of the meniscus and the contact angle as a function of liquid uptake or liquid release** in the pore system.

Different capillary pressures are associated with each of these meniscus shapes, which can differ significantly in the adsorption and desorption phases. Nevertheless, no influence on the hysteretic behavior of the moisture storage can be derived from these transient phases, since the respective equilibrium states are assigned to this behavior with the associated stationary menisci and contact angles. The condensate volume at the inner pore surfaces of the pore system forms according to Section 1.4, and because of the small influence of the discussed relation on the pore radii, **the dependencies between pore radius and capillary pressure or of Section 1.3 should be applied unchanged.**

References

- 1 Thommes, M., Kaneko, K., Neimark, A.V. et al. (2015). Physisorption of gases, with special reference to the evaluation of surface area and pore size distribution (IUPAC Technical Report). *Pure and Applied Chemistry* 87: 160.
- 2 Fagerlund, G. (2004). A Service Life Model for Internal Frost Damage in Concrete. Division of Building Materials. *Report TVBM*; Vol. 3119. Lund University.
- 3 Eriksson, D., Gasch, T., and Ansell, A. (2018). A hygro-thermo-mechanical multiphase model for long-term water absorption into air-entrained concrete. *Transport in Porous Media* 20: 573.
- 4 Carmeliet, J. and Roels, S. (2002). Determination of the moisture capacity of porous building materials. *Journal of Building Physics* 25: 209–237.

- 5 Krus, M. (1996). Moisture transport and storage coefficients of porous mineral building materials: theoretical principles and new test methods. *Reprint Dissertation (Stuttgart University) by Fraunhofer IRB Verlag.*
- 6 Scheffler, G.A. (2008). Validierung hygrothermischer Materialmodellierung unter Berücksichtigung der Hysterese der Feuchtespeicherung. Dissertation. Technische Universität Dresden.
- 7 Espinosa, R.M. and Franke, L. (2006). Inkbottle Pore-Method: prediction of hygroscopic water content in hardened cement paste at variable climatic conditions. *Cement and Concrete Research* 36: 1954–1968.
- 8 Feldman, R.F. and Sereda, P.J. (1968). A model for hydrated Portland cement paste as deduced from sorption-length change and mechanical properties. *Materiaux et Constructions* 1: 509–520.
- 9 Ahlgren, L. (1972). Moisture Fixation in Porous Building Materials. *Report 36.* The Lund Inst. of Technology.
- 10 Welcome to DataPhysics-Instruments (2019). *Collection of Surface-Tension values of Liquids and Solids.* www.dataphysics-instruments.com (accessed 27 December 2023).
- 11 Pérez-Díaz, J.L., Álvarez-Valenzuelab, M.A., and García-Pradab, J.C. (2012). The effect of the partial pressure of water vapor on the surface tension of the liquid water–air interface liquid water–air interface. *Journal of Colloid and Interface Science* 381 (1): 180–182.
- 12 Portuguez, E., Alzina, A., Michaud, P. et al. (2017). Evolution of a water pendant droplet: effect of temperature and relative humidity. *Natural Science* 9: 1–20.
- 13 Chen, H., Li, Z., Wang, F. et al. (2017). Extrapolation of surface tensions of electrolyte and associating mixtures solutions. *Chemical Engineering Science* 162: 10–20.
- 14 Kinloch, A.J. (1980). Review the science of adhesion Part 1 : Surface and interfacial/aspects. *Journal of Materials Science* 15: 2141–2166.
- 15 van Honschoten, J.W., Brunets, N., and Tas, N.R. (2010). Capillarity at the nanoscale. *Chemical Society Reviews* 39: 1096–1114.
- 16 Barnat-Hunek, D. and Smarzewski, P. (2015). Surface free energie of hydrophobic coatings of hybrid-fiber-reinforced high-performance concrete. *Materiali in Tehnologije / Materials and Technology* 49: 895–902.
- 17 Kumikov, V.K. and Khokonov, K.B. (1983). On the measurement of surface free energy and surface tension of solid metals. *Journal of Applied Physics* 54: 1346–1350.
- 18 Yuan, Y. and Lee, T.R. (2013). Contact angle and wetting properties. In: *Surface Science Techniques, Springer Series in Surface Sciences 51.* Springer.
- 19 Lauth, G.-J. and Kowalczyk, J. (2016). *Einführung in die Physik und Chemie der Grenzflächen und Kolloide. Experimentelle Methoden: Messung der Grenzflächenspannung.* Springer-Spektrum.
- 20 Cwikel, D., Zhao, Q., Liu, C. et al. (2010). Comparing contact angle measurements and surface tension assessments of solid surfaces. *Langmuir* 26 (19): 15289–15294.

- 21 Extrand, C.W. and Moon, S.I. (2012). Which controls wetting? Contact line versus interfacial area: simple experiments on capillary rise. *Langmuir-Journal of the American Chemical Society* 28: 15629–15633.
- 22 Matsuoka, H., Fukui, S., and Kato, T. (2002). Nanomeniscus forces in under-saturated vapors: observable limit of macroscopic characteristics. *Langmuir* 18: 6796–6801.
- 23 Kim, S., Kim, D., Kim, J. et al. (2018). Direct evidence for curvature-dependent surface tension in capillary condensation: Kelvin equation at molecular scale. *Physical Review X* 8: 041046.
- 24 Blokhuis, E.M. and Kuipers, J. (2006). Thermodynamic expressions for the Tolman length. *Journal of Chemical Physics* 124: 74701.
- 25 Eslami, F. and Elliott, J.A.W. (2019). Gibbsian thermodynamic study of capillary meniscus depth. *Scientific Reports* 9: 657.
- 26 Maris, H. and Balibar, S. (2000). Negative pressures and cavitation in liquid helium. *Physics Today, American Institute of Physics* 53 (2): 29–34.
- 27 Caupin, F., Arvengas, A., Davitt, K. et al. (2012). Exploring water and other liquids at negative pressure. *Journal of Physics: Condensed Matter* 24: 284110
- 28 Israelachvili, J.N. (2011). *Intermolecular and Surface Forces*, 3e. Elsevier.
- 29 Rouquerol, F., Rouquerol, J., and Sing, K.S. (2014). *Adsorption by Powders and Porous Solids, Principles, Methodology and Applications*. Elsevier.
- 30 Adolphs, J. and Setzer, M.J. (1996). A model to describe adsorption isotherms. *Journal of Colloid and Interface Science* 180: 70–76.
- 31 Brunauer, S., Emmett, P.H., and Teller, E.J. (1938). Adsorption of gases in multi-molecular layers. *Journal of the American Chemical Society* 60: 309.
- 32 Badmann, R., Stockhausen, N., and Setzer, M.J. (1981). The statistical thickness and the chemical potential of adsorbed water films. *Journal of Colloid and Interface Science* 82: 534–542.
- 33 Zandavi, S.H. and Ward, C.A. (2014). Clusters in the adsorbates of vapours and gases: Zeta isotherm approach. *Physical Chemistry Chemical Physics* 16: 10979–10989.
- 34 Zandavi, S.H. (2015). Vapours adsorption on non-porous and porous solids: Zeta Adsorption Isotherm Approach. Dissertation. University of Toronto.
- 35 Funk, M. (2012). Hysteresis der Feuchtespeicherung in porösen Materialien. Dissertation. Technische Universität Dresden.
- 36 deBoer, J.H., Linsen, B.G., and Osinga, T.J. (1965). Studies on pore systems in catalysis. VI. The universal t-curve. *Journal of Catalysis* 4(6): 643–648.
- 37 Snoeck, D., Velasco, L.F., Mignon, A. et al. (2014). The influence of different drying techniques on the water sorption properties of cement-based materials. *Cement and Concrete Research* 64: 54–62.
- 38 Kumar, A., Ketel, S., Vance, K. et al. (2014). Water vapor sorption in cementitious materials—measurement, modeling and interpretation. *Transport in Porous Media* 103: 69–98.
- 39 Brunauer, S., Skalny, J., and Bodor, E.E. (1969). Adsorption on nonporous solids. *Journal of Colloid and Interface Science* 30: 546–552.

- 40 Pavlik, Z., žumár, J., Medved, I., and Černý, R. (2012). Water vapor adsorption in porous building materials: experimental measurement and theoretical analysis. *Transport in Porous Media* 91: 939–954.
- 41 Adolphs, J. and Setzer, M.J. (1996). Energetic classification of adsorption isotherms. *Journal of Colloid and Interface Science* 184: 443–448.
- 42 Adolphs, J. and Setzer, M.J. (1998). Description of gas adsorption isotherms on porous and dispersed systems with the excess surface work model. *Journal of Colloid and Interface Science* 207: 349–354.
- 43 Ridgway, C.J., Schoelkopf, J., Matthews, G.P. et al. (2001). The effects of void geometry and contact angle on the absorption of liquids into porous calcium carbonate structures. *Journal of Colloid and Interface Science* 239: 417–431.
- 44 Wu, C., Zandavi, S.H., and Ward, C.A. (2014). Prediction of the wetting condition from the Zeta adsorption isotherm. *Physical Chemistry Chemical Physics* 16: 25564–25572.
- 45 Churaev, N., Starke, G., and Adolphs, J. (2000). Isotherms of capillary condensation influenced by formation of adsorption films. *Journal of Colloid and Interface Science* 221: 246–253.
- 46 Mattia, D., Starov, V., and Semenov, S. (2012). Thickness, stability and contact angle of liquid films on and inside nanofibres, nanotubes and nanochannels. *Journal of Colloid and Interface Science* 384 (1): 149–156.
- 47 Li, J., Li, X., Wu, K. et al. (2016). Water sorption and distribution characteristics in clay and shale: effect of surface force. *Energy Fuels* 30: 8863–8874.
- 48 Teletzke, G.F. and Davis de L.E. Scriven, H.T. (1988). Wetting hydrodynamics. *Physical Review Applied* 23: 989–1007.
- 49 Kruk, M. and Jaroniec, M. (2002). Determination of mesopore size distributions from argon adsorption data at 77 K. *Journal of Physical Chemistry B* 106: 4732–4739.
- 50 Zhang, Y., Ouyang, X., and Yang, Z. (2019). Microstructure-based relative humidity in cementitious system due to self-desiccation. *Materials* 12: 1214.
- 51 Dash, J.G. and Peierls, R. (1982). Characteristics of adsorbed films. *Physical Review B* 25: 8.
- 52 Churaev, N.V., Setzer, M.J., and Adolphs, J. (1998). Influence of surface wettability on adsorption isotherms of water vapor. *Journal of Colloid and Interface Science* 197: 327–333.
- 53 Zhao, G., Tan, Q., Xiang, L. et al. (2015). Structure and properties of water film adsorbed on mica surfaces. *Journal of Chemical Physics* 143: 104705.
- 54 Xu, S., Simmons, G.C., Mahadevan, T.S. et al. (2009). Transport of water in small pores. *Langmuir* 25: 5084–5090.
- 55 Gruener, S., Hofmann, T., Wallacher, D. et al. (2009). Capillary rise of water in hydrophilic nanopores. *Physical Review E-APS* 79: 1–5.
- 56 Wu, K., Chen, Z., Li, J. et al. (2017). Wettability effect on nanoconfined water flow. *Proceedings of the National Academy of Sciences of the United States of America* 114 (13): 3358–3363.

- 57 Antognozzi, M., Humphris, A.D.L., and Miles, M.J. (2001). Observation of molecular layering in a confined water film and study of the layers viscoelastic properties. *Applied Physics Letters* 78 (3): 300–302.
- 58 Arai, T., Sato, K., Iida, A., and Tomitori, M. (2017). Quasi-stabilized hydration layers on muscovite mica under a thin water film grown from humid air. *Scientific Reports* 7: 4054.
- 59 Aktulga, H.M., Fogarty, J.C., Pandit, S.A., and Grama, A.Y. (2012). Parallel reactive molecular dynamics: numerical methods and algorithmic techniques. *Parallel Computing* 38: 245–259.
- 60 Farah, K., Müller-Plathe, F., and Böhm, M.C. (2012). Classical reactive molecular dynamics implementations: state of the art. *ChemPhysChem* 13: 1127–1151.
- 61 Castrillon, S.R.-V., Giovambattista, N., Aksay, I.A., and Debenedetti, P.G. (2011). Structure and energetics of thin film water. *Journal of Physical Chemistry C* 115: 4624–4635.
- 62 Israelachvili, J., Min, Y., Akbulut, M. et al. (2010). Recent advances in the surface forces apparatus (SFA) technique. *Reports on Progress in Physics* 73: 036601.
- 63 Peng, J., Guo, J., Ma, R., and Jiang, Y. (2022). Water-solid interfaces probed by high-resolution atomic force microscopy. *Surface Science Reports* 71: 100549.
- 64 Fukuma, T. (2015). Mechanism of atomic force microscopy imaging of three-dimensional hydration structures at a solid-liquid interface. *Physical Review B* 92: 155412.
- 65 Monroe, J., Barry, M., DeStefano, A. et al. (2020). Water structure and properties at hydrophilic and hydrophobic surfaces. *Annual Review of Chemical and Biomolecular Engineering* 11: 523–557.
- 66 Asay, D.B. and Kim, S.H. (2005). Evolution of the adsorbed water layer structure on silicon oxide at room temperature. *Journal of Physical Chemistry B* 109: 16760–16763.
- 67 Kimura, K., Ido, S., Oyabu, N. et al. (2010). Visualizing water molecule distribution by atomic force microscopy. *Journal of Chemical Physics* 132: 194705.
- 68 Martin-Jimenez, D., Chacon, E., Tarazona, P., and Garcia, R. (2016). Atomically resolved three-dimensional structures of electrolyte aqueous solutions near a solid surface. *Nature Communications* 7: 12164.
- 69 Lothenbach, B., Winnefeld, F., Alder, C. et al. (2007). Effect of temperature on the pore solution, microstructure and hydration products of Portland cement pastes. *Cement and Concrete Research* 37: 483–491.
- 70 Kenny, A. and Katz, A. (2020). Cement composition's effect on pore solution composition and on electrochemical behavior of reinforcing steel. *Israel Institute for Technology, Haifa, Israel, Reprint*.
- 71 Kuchin, I.V., Matar, O.K., Craster, R.V., and Starov, V.M. (2014). Modeling the effect of surface forces on the equilibrium liquid profile of a capillary meniscus. *Soft Matter* 10: 6024–6037.
- 72 Kuchin, I.V. and Starov, M. (2016). Hysteresis of the contact angle of a meniscus inside a capillary with smooth, homogeneous solid walls. *Langmuir* 32: 5333–5340.

- 73** Zhang, T., Li, X., Sun, Z. et al. (2017). An analytical model for relative permeability in water-wet nanoporous media. *Chemical Engineering Science* 174: 1–12.
- 74** Wang, F.-C. and Zhao, Y.-P. (2011). Slip boundary conditions based on molecular kinetic theory: the critical shear stress and the energy dissipation at the liquid–solid interface. *Soft Matter* 7: 8628–8634.
- 75** Feng, D., Li, X., Wang, X. et al. (2018). Capillary filling of confined water in nanopores: coupling the increased viscosity and slippage. *Chemical Engineering Science* 186: 228–239.
- 76** Schimmele, L., Napiórkowski, M., Dietrich, S. et al. (2007). Conceptual aspects of line tensions. *Journal of Chemical Physics* 127: 164715.
- 77** Starov, V.M. and Velarde, M.G. (2009). Surface forces and wetting phenomena. *Journal of Physics: Condensed Matter* 21: 464121.
- 78** Andrew, M., Bijeljic, B., and Blunt, M.J. (2014). Pore-scale contact angle measurements at reservoir conditions using X-ray microtomography. *Advances in Water Resources* 68: 24–31.
- 79** Siebold, A., Walliser, A., Nardin, M. et al. (1997). Capillary rise for thermodynamic characterization of solid particle surface. *Journal of Colloid and Interface Science* 186: 60–70.
- 80** Popescu, M.N., Ralston, J., and Sedev, R. (2008). Capillary rise with velocity-dependent dynamic contact angle. *Langmuir* 24: 12710–12716.